Journal of Materials Chemistry C

Charge Generation Mechanism Tuned via Film Morphology in Small Molecule Bulk-Heterojunction Photovoltaic Materials

Journal:	*Journal of Materials Chemistry C*
Manuscript ID	TC-ART-07-2020-003393.R1
Article Type:	Paper
Date Submitted by the Author:	08-Aug-2020
Complete List of Authors:	Lou, Sylvia; Northwestern University, Department of Chemistry Loser, Stephen; Northwestern University, Department of Chemistry Luck, Kyle; Northwestern University, Chemistry Zhou, Nanjia; Westlake University, Leonardi, Matthew; Northwestern University, Department of Chemistry Timalsina, Amod; Northwestern University, Department of Chemistry Manley, Eric; Northwestern University, Chemistry Hayes, Dugan; University of Rhode Island College of Arts and Sciences, Department of Chemistry Strzalka, Joseph; Argonne National Laboratory, X-Ray Science Division; X-Ray Science Division, Argonne Hersam, Mark; Northwestern University, Department of Materials Science and Engineering Chang, Robert; Northwestern University, Department of Materials Science and Engineering Marks, Tobin; Northwestern University, Department of Chemistry Chen, Lin; Northwestern University, Chemistry; Argonne National Laboratory, Chemical Sciences and Engineering

Charge Generation Mechanism Tuned via Film Morphology in Small Molecule Bulk-Heterojunction Photovoltaic Materials

Sylvia J. Lou,[1] Stephen Loser,[1] Kyle A. Luck,[1] Nanjia Zhou,[1] Matthew J. Leonardi,[1] Amod Timalsina,[1] Eric F. Manley,[1] Dugan Hayes,[2] Joseph Strzalka,[3] Mark C. Hersam,[1,4] Robert P.H. Chang,[4] Tobin J. Marks[1]*, Lin X. Chen[1,2]*

[1]Department of Chemistry, Northwestern University, Evanston, Illinois 60208, USA
[2]Chemical Science and Engineering Division, Argonne National Laboratory, Lemont, Illinois 60439, USA
[3]X-ray Science Division, Advanced Photon Source, Argonne National Laboratory, Lemont, Illinois 60439, USA
[4]Department of Materials Science and Engineering, Northwestern University, Evanston, Illinois 60208, USA

Abstract

Small organic molecules have emerged as promising component materials for organic photovoltaic devices. Compared to most conjugated polymers for the same application, small molecules have unique morphologies that promote electronic processes relevant to organic solar cell (OSC) function that can be significantly different from those of conjugated polymeric materials. Here we investigate constituent loading-dependent effects on OSC morphology and function using the classical fullerene acceptor, $PC_{61}BM$, in a heterojunction blend with the small molecule donor, NDT (thiophene-capped diketopyrrolopyrrole naphthodithiophene). The evolution of active layer morphology as well as exciton speciation and dynamics as a function of the $PC_{61}BM$ content are examined in combined structural studies using GIWAXS and spectroscopic studies using transient absorption spectroscopy. We observe evidence for three types of coexisting excitons and details of the interplay between them determines the yield of charge separated states that afford sustained device efficiency.

Introduction

Over the past decade, the general consensus concerning the mechanism of charge generation in bulk-heterojunction (BHJ) organic photovoltaics (OPVs) has steadily evolved, resulting in multiple theories of charge separation/generation.[1-10] While initial understandings were developed using the P3HT donor polymer and its derivatives,[11-14] ultrafast (<100 fs) charge generation was observed,[15-20] in polymers consisting of linked electron-rich and electron-poor subunits, necessitating the development of theories to include such intramolecular electronic "push-pull" effects in exciton and charge generation dynamics.[4,21-23] Although conjugated small organic molecules exhibit many similarities to their polymer counterparts, the relative importance of energetic and morphological variables in the charge generation process is expected to vary based on the differences in both molecular structure and bulk morphology. In this work, holding the fullerene molecular acceptor $PC_{61}BM$ constant, we focus on elucidating the relationship between donor molecular structure, donor-acceptor interactions, bulk morphology, and the resulting charge generation and recombination kinetics, which may have significant implications for other small molecule OPV materials including both the electron donor and acceptor.

There are different models used to describe the mechanisms of charge generation from the exciton splitting in BHJ active layer, but they are united in a primary emphasis on electronic processes at the donor/acceptor interface: the donor and acceptor electronic state energetics, the electrostatic interactions between holes and electrons, and charge generation dynamics; as well as in a secondary emphasis on morphology effects on the energy landscape at the donor/acceptor interface.[1,2,8,24,25] General to almost all these descriptions is that an exciton is created in the donor/acceptor domain and then diffuses or hops to an interface where due to the energetic offset between the donor and acceptor, the exciton delocalizes across the interface to form a charge

transfer (CT) state in which the hole in the donor domain and the electron in the acceptor domain at the domain boundary are strongly interacting, then from the CT state the hole and electron separate further to form a charge separated, CS, state, and then finally evolve into free carriers. Alternatively, the hole and electron at the donor-acceptor interface can recombine back to the ground state, a mechanism for the loss of PV efficiency. In polymers, excitons and charge diffusion/hopping may occur through π-stacked backbones and along the π-conjugated backbone,[26,27] while small molecules lack the long range π-conjugation and thus require adequate crystallinity and conduction across grain boundaries to enable these processes.[28] It has been suggested that the optimum domain size in the BHJ films should be about 10 nm in order for an exciton in the conjugated organic materials to reach a donor-acceptor interface before decay,[29-31] so most BHJ solar cells have typically been optimized via synthesis and film processing, to achieve donor domains of ~10 nm. However, more recent studies have found excellent solar cell performance with domains up to five times larger than the 10 nm limit.[32-36] In addition, the time scale for the free charge carrier generation processes has been reported to take place on the picosecond time scale,[25,37] while the exciton splitting dynamics of several high-efficiency push-pull polymers have been remarkably bracketed by CS state formation in <100 fs.[15-17]

To explain the essentially "instantaneous" exciton splitting and CS state formation, the "hot exciton" model was proposed in which photoexcitation results in an initially highly delocalized exciton[25,38] in a state energetically comparable to excited, and delocalized, charge transfer states, which would thus enable the ultrafast exciton splitting.[16,39-46] Some studies also suggest that it is possible to directly excite delocalized charge transfer excitons having decreased Coulombic attraction compared to the corresponding lower energy localized states.[47-49] These models have been experimentally demonstrated in numerous polymer systems,[50-52] but only explicitly studied

theoretically in small molecule systems,[28,53-55] even though ultrafast charge generation has also been observed in small molecule donor systems.[43,56-58] Unlike the exciton diffusion model, it appears that a high degree of crystallinity in the small molecule domains must be present in order to form the necessary high energy delocalized CT states.[8,59-62] In contrast to this picture, high degrees of polymer ordering may not be required since the delocalized exciton could form/be stabilized in the π-systems along the conjugated polymer backbones.[63-65]

Both of the above models have implications for the bulk morphology of a solar cell thin film active layer, and acknowledge the large effect the local morphology at the interface has on the interfacial energy states. A number of theoretical studies have proposed that the ideal location/orientation of fullerene molecules between conjugated molecules and oligomers places the π-conjugated faces aligned in parallel with each other.[66-72] Other studies have computed the interfacial charge transfer molecular orbitals and their energies and find that at the interfaces, the bulk energetics measured in pure domains may be inaccurate due to electrostatic interactions between the donor and fullerene frontier orbitals.[73-75] Several studies on the influence of disorder at the interface suggest that disorder may have an effect on charge generation suggesting that the charge transfer state is larger than the neighboring interfacial area[71,72,76,77] while other studies indicate that an ordered interface promotes charge generation, but also allows for fast geminate charge recombination if only the localized charge transfer state is available at the interface.[78,79] The effects of interfacial molecular structure on exciton splitting and charge searation dynamics, therefore, remain a matter of debate and are likely highly system-specific.

While geminate charge recombination is intimately linked to the local interfacial structure, the morphology of the pure domains and bulk thin film are key determinates for charge transport processes which affect bimolecular recombination. Assuming adequate $PC_{61}BM$ loading, a

number of studies have shown that the $PC_{61}BM$ easily forms interconnected networks which facilitates electron transport to the electrode.[46,61-63] Similarly, most polymers form networks of pure polymer domains connected via polymer backbones to adequately transport holes to the electrodes[80,81] despite low hole mobilities due to amorphous or weakly crystalline/ordered domains.[65,82] If the bimolecular recombination dynamics are faster than the charge transport dynamics, losses in solar cell efficiency occur. However, small donor molecules have the potential to achieve greater purity, monodispersity, order/crystallinity, and large hole and electron mobilities to facilitate rapid charge extraction, but on the other hand, are more likely to form isolated donor islands[83] and/or donor domain boundaries that energetically restrict charge transport across domains,[84,85] and thereby create charge traps which increase bimolecular recombination.

In this study, we investigate the influence of donor crystallinity in a previously published thiophene-capped diketopyrrolopyrrole (TDPP) naphthodithiophene (NDT) based TDPP-NDT-TDPP small molecule electron donor (Figure 1).[86,87] This molecule has an acceptor-donor-acceptor (*ada*) arrangement where naphthodithiophene and TDPP are respectively electron donating and accepting moieties within the donor structure (for the sake of brevity, the entire TDPP-NDT-TDPP molecule will simply be called NDT throughout this report). NDT, as an electron donor (D) material, is paired with electron acceptor (A) $PC_{61}BM$ in the active layer BHJ films for the OPV devices, and the morphology of the films are tuned by varying the $PC_{61}BM$ loading from 0% to 80% $PC_{61}BM$ by weight.[87-89] The relative degree of crystallinity of NDT at each $PC_{61}BM$ loading is determined by X-ray structural studies from which we can deduce relative orientations of NDT and $PC_{61}BM$ using an experimental crystal structure as reference.[89] The corresponding charge separation and recombination dynamics were measured using transient absorption spectroscopy and correlated with the solar cell efficiencies. From these results, we can establish three different

relationships between charge generation and morphology that are dependent on $PC_{61}BM$ loading, and suggest key parameters for enhancing solar cell efficiency in the NDT:$PC_{61}BM$ active layer. The findings reveal the correlation between BHJ film morphology and the dynamics of exciton splitting and charge diffusion as well as the interplays of different structural factors that influence the small molecule OPV device performance.

Methods

Synthesis and device fabrication. The synthesis for the NDT donor molecule (Figure 1A) has been previously reported.[87] Solutions of different $PC_{61}BM$ loadings were based on weight:weight ratios of NDT:$PC_{61}BM$. The NDT and $PC_{61}BM$ solutions were stirred on a covered hot plate at 40°C in a dry N_2 glovebox, and the NDT concentration was held constant for all solutions. Device fabrication has been previously reported[87] with the addition that all tested samples were either studied as deposited or annealed at 130°C, resulting in a final conventional device architecture of ITO/PEDOT-PSS/NDT:$PC_{61}BM$/LiF/Al. The solar cell performance was measured using a Spectra-Nova Class A solar simulator under a calibrated AM1.5G light (100 mW/cm^2) using a Xe arc lamp. The EQE was also measured and used to correct the J_{sc}. Solar cell dimensions were 0.06 cm^2.

Grazing incidence x-ray scattering. Grazing incidence x-ray scattering (GIXS) was performed at Beamline 8-ID-E[90] of the Advanced Photon Source at Argonne National Laboratory. The beam energy was 7.35 keV with a spot size of 0.02 mm x 0.2 mm. Data were collected using a 2D Pilatus 1M pixel array detector at a sample-detector distance of 204 mm for wide-angle scattering (GIWAXS) and 2164 mm for small-angle scattering (GISAXS). Each sample was exposed at an incident angle of 0.2° for 20 seconds. The data were summed and a mask and flat field correction

were applied using the GIXSGUI package[91] for Matlab. Two dimensional linecuts were taken 10±10 pixels to the right or above the beamspot parallel to the q_z or q_{xy} axis, and the background was subtracted by fitting to an exponential decay. Peaks were fit using a Gaussian multipeak fitting procedure with the average peak width and noise specified by the initial conditions.

Optical transient absorption (OTA) spectroscopy. Optical femtosecond transient absorption (fs TA) measurements were performed using an amplified Ti:sapphire laser system. A 1-kHz, amplified 830 nm beam with pulse energy of 3 mJ was generated by a Spitfire Pro XP regenerative amplifier (Spectra-Physics) which was pumped by an Empower Nd:YLF laser (Spectra-Physics) with a seed beam generated by a Mai Tai Ti:sapphire oscillator (Spectra-Physics). The majority of the 830 nm amplifier output was used to generate the pump beam via a home-built, white light-seeded OPA, and the remaining output was used to generate the white light probe in a Helios transient absorption spectrometer (Ultrafast Systems) by focusing the beam into a thin sapphire plate (for visible detection) or a proprietary crystal (for near IR detection). The pump wavelength was tuned to 530 nm for solution samples and 600 nm for film samples. The laser pulse energy at the sample was 20 nJ at the sample, and the pump-probe repetition rate was at 500 Hz. The pump beam was focused to a 100 μm beam diameter at the sample resulting in a fluence of 30 μJ/cm^2. The instrument response function was 240 fs (FWHM). The white light probe was detected by a CMOS camera with an integration time of 3 seconds per spectrum. These experiments were conducted at room temperature under a nitrogen gas flow. Four to five scans were averaged, and samples were moved between scans to minimize photodegradation.

Results

In this section, we present our combined studies correlating the active layer with the different steps of OPV function from initial exciton dynamics to charge carrier generation and ultimately device performance. We start from the crystal structure of NDT and relate it to the thin film structure as determined by grazing incidence wide-angle X-ray scattering (GIWAXS). Using the simulated powder diffraction from the single crystal structure, we assign the scattering features and determine the relative orientation of the NDT crystallite in the thin film by GIWAXS measurements. Then the GIWAXS scattering patterns are compared for thin films of neat NDT and NDT:$PC_{61}BM$ blend films for a $PC_{61}BM$ of 0.1, 1, 10, 20, 30, 40, 50, 60, and 80% w/w loading. Changes in peak amplitude, d-spacing, and coherence length (CL) were calculated via Scherrer analysis[92] to provide insight into the interfacial orientations between NDT and $PC_{61}BM$ as well as the thin film morphology. As the morphology changes, we then determine effects of $PC_{61}BM$ loading on charge generation and recombination using optical femtosecond and nanosecond transient absorption spectroscopy. In particular, we examine the effects of intra- and inter-molecular/domain charge transfer properties as a function of the morphology tuned by varying the $PC_{61}BM$ loading. Finally, these photophysical and morphological characterization results are correlated with the corresponding solar cell performance to rationalize the optimal morphology for the optimal performance.

1. Single crystal structure.

The single crystal structure of NDT has been previously published.[89] Here we highlight the important features and definitions relevant to this study. The single crystal exhibits a slip-stacked structure in which the molecules are π-π stacked in columns with the backbone offset by ~5 Å (Figure 1). We attribute the degree of backbone offset to the orientation of the side chains, but note that the structure solution for the side chains has a high degree of uncertainty (Figure 1A).

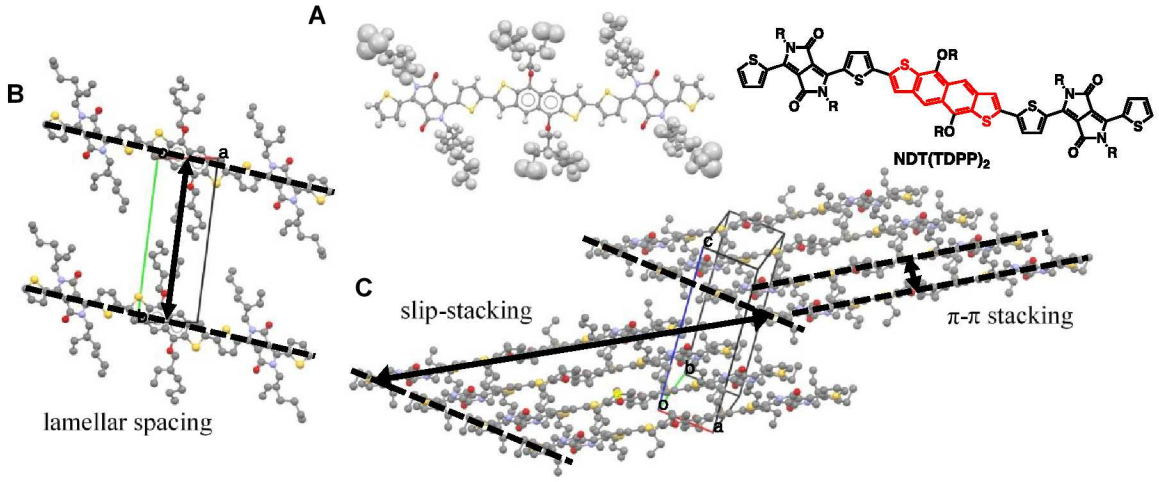

Figure 1. A. NDT [NDT(TDPP)$_2$] molecular structure, B and C. Single crystal structure of NDT molecule with relevant intermolecular interactions.

The molecules are arranged diagonally across the unit cell such that the relevant intermolecular interactions (slip-stack spacing, lamellar spacing, and π-π stacking) are not simply related to the unit cell axes (Figures 1B&1C). The implications of this will be discussed in more detail below.

2. *Grazing incidence X-ray scattering* (GIXS)

Because the active layers in organic solar cells are either spin coated or printed, neat NDT thin films are consist of small crystallite domains. Using GIXS (GIWAXS and GISAXS), we first examined the film morphology for neat and blend samples with and without annealing effects on their morphology, then investigated the impact of $PC_{61}BM$ loading.

2.1. *Neat NDT and blend NDT:$PC_{61}BM$ thin films without and with annealing*

The crystallite structures of neat NDT and NDT:$PC_{61}BM$ blends were measured by GIWAXS using a 2D pixel array detector (Figure 2). The image of the unannealed neat film exhibits five distinct arcs of diffraction demonstrating the formation of NDT crystallites (Figure 2A). Three regularly-spaced diffraction arcs are visible originating from the q_z axis while the other two arcs originate along the q_{xy} axis. These arcs are anisotropic, indicating the texture present in

the film, a non-uniform distribution of NDT crystallite orientations, consistent with a predominantly edge-on molecular orientation relative to the substrate. Upon annealing the neat NDT film at 130°C, an increase in the intensities of the diffraction peaks is observed, indicating an increase of the NDT crystallinity (Figure 2B). The addition of $PC_{61}BM$ at 40% loading reduces the NDT crystallinity dramatically in the unannealed film (Figure 2C), but the NDT crystallinity again increases with annealing in the blend film (Figure 2D), although the NDT domains in the blend film exhibit decreased crystallinity compared to the neat NDT film. In addition, the unannealed blend film exhibits only one isotropic $PC_{61}BM$ ring at q = 1.4 $Å^{-1}$ while the annealed film exhibits a second $PC_{61}BM$ ring at q = 0.7 $Å^{-1}$, indicating that annealing also leads to increased $PC_{61}BM$ crystallinity.

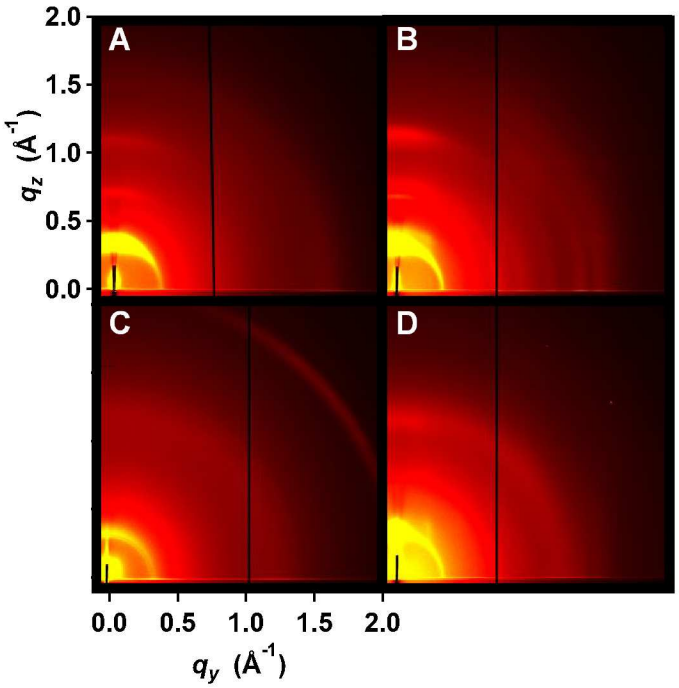

Figure 2. 2D images of X-ray scattering of films of A) Unannealed neat NDT, B) Neat NDT annealed at 130°, C) Unannealed NDT + 40% $PC_{61}BM$, and D) NDT + 40% $PC_{61}BM$ annealed at 130°C. GIWAXS data recorded with the same exposure time and displayed with the same false color intensity scale. The scales of axes for all panels are the same as labeled in A) and C).

Scattering intensity along the q_{xy} axis signifies diffraction in the plane parallel to the substrate while intensity along the q_z axis signifies diffraction perpendicular to the substrate plane. The parallel (in-plane) and perpendicular (out-of-plane) components were isolated by linecuts parallel to the q_{xy} and q_z axes, respectively (Figure 3). The qualitative similarity between the simulated powder diffraction from the single crystal structure and the thin film structure suggests that the NDT crystallizes in the same unit cell in thin film. We note that the diffraction peaks of

the NDT crystallites in thin film are slightly shifted to larger q values than the single crystal simulated powder diffraction. Since q is inversely related to d-spacing ($q = 2\pi/d$) this indicates a slightly smaller unit cell (~5%) in the thin film than the single crystal which is not uncommon.[93]

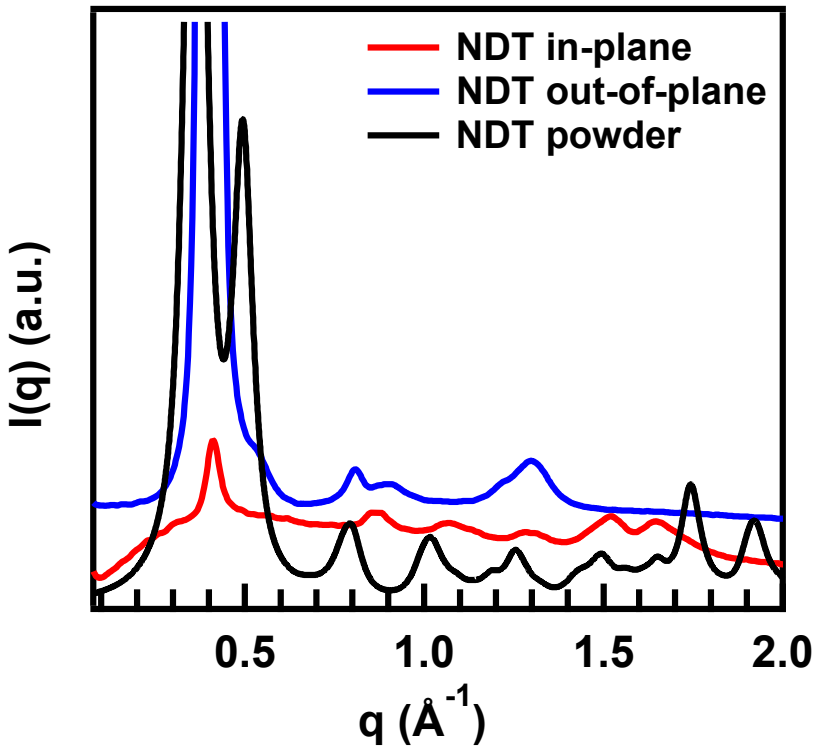

Figure 3. In-plane and out-of-plane linecuts describing the annealed NDT thin film structure in comparison to the powder diffraction calculated from the single crystal structure.

The peaks were fit using a multiple Gaussian peak fitting procedure to obtain the peak location and width, which is later used to calculate the coherence length (CL) using a modified Scherrer analysis.[92] Through comparison to the simulated powder diffraction, we assign the diffraction planes to the GIWAXS peaks as given in Table 1.

Table 1. Primary intermolecular interactions determined from the single crystal structure, scattering vectors, and CLs of NDT and $PC_{61}BM$ in annealed and (unannealed) thin films as determined by GIWAXS.

Diffraction Peak*	**1° intermol. interaction**	**q_{powder} [Å^{-1}]**	**q_{neat} ann. (unann.) [Å^{-1}]**	**$q_{6:4}$ ann. (unann.) [Å^{-1}]**	**CL_{neat} ann. (unann.) [nm]**	**$CL_{6:4}$ ann. (unann.) [nm]**	**CL_{PC61BM}**
(010)	*m*	0.37	0.41 (0.39)	0.41 (0.41)	19.4 (10.9)	13.7 (8.3)	---
(02$\bar{1}$)	*l*	0.80	0.85 (0.91)	---	3.6 (15.5)	---	
(02$\bar{2}$)	*l, s*	0.99	1.07	0.87	4.5	49.5	
(1$\bar{2}\bar{1}$)	*s, p*	1.19	1.29	---	3.7	---	
(112)	*m*	1.26					
(033)	*m*	1.50	1.51 (1.51)	1.53	6.3 (11.9)	16.0	
(122)	*s*	1.50					
(1$\bar{2}\bar{4}$)	*p*	1.74	1.64 (1.67)	1.66	5.4 (4.2)	8.4	
(001)**	*m*	0.34	0.39 (0.39)	0.40 (0.40)	21.2 (10.0)	12.2 (5.0)	---
(01$\bar{2}$)**	*s*	0.77	0.79 (0.80)	---	17.7 (4.6)	---	
(02$\bar{1}$)**	*l*	0.80	0.88	0.90	5.9	11.8	
(1$\bar{1}\bar{2}$)**	*s, p*	1.19	1.27 (1.21)	1.31	3.6 (4.7)	NA	
(023)**	*s*	1.26	1.31 (1.33)	NA	8.2 (15.7)	10.5	
$PC_{61}BM$ (111)	NA	0.76	NA	0.76	NA	NA	3.6
$PC_{61}BM$ (311)		1.34		1.39 (1.33)			1.9 (1.3)
$PC_{61}BM$ (111)**		0.76		0.78 (NA)			4.5
$PC_{61}BM$ (311)**		1.34		1.35 (1.35)			2.7 (1.9)

*Diffraction peaks related to the end-on stacking on noted in **bold** and **Diffraction peaks located along the q_z axis.

We relate the diffraction planes to the intermoecular interactions (π-π stacking (*p*), lamellar spacing (*l*), and slip stack spacing (*s*)) by expressing the diffraction plane as a linear combination of the vectors describing the molecular dimensions. Although most of the diffraction planes consist of a mixture (*m*) of at least two of the intermolecular interactions, we selected five diffraction planes which primarily define a single intermolecular interaction: lamellar spacing (02$\bar{1}$), slip stack spacing (122), (112), and (023), and π-π spacing (1$\bar{2}\bar{4}$) (Figure 4).

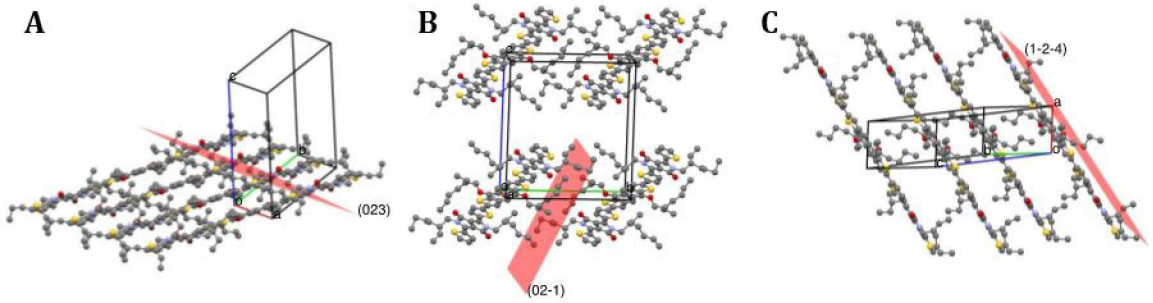

Figure 4. Planes describing relevant intermolecular interactions (A) End-on or slip-stacking interaction (023), (B) lamellar interaction (02$\bar{\mathbf{1}}$), and (C) π-π stacking interaction (1 $\bar{\mathbf{2}}\bar{\mathbf{4}}$).

Diffraction (023) appears only in the out-of-plane linecut; (122), (112), and (1$\bar{2}\bar{4}$) are visible only in the in-plane linecut; and (02$\bar{1}$) is present in both linecuts. All of these peaks are present in the unannealed and annealed neat NDT films, but the *d*-spacing in the unannealed film is larger than the annealed film indicating a compression of the unit cell upon annealing (Table 2). Most of these peaks appear in the 2D image as anisotropic rings with their highest intensity along the q_{xy} or q_z axes. Depending on the location of highest intensity, the peaks describe either an end-on (noted in bold font in Table 2) or side-on (non-bold font in Table 2) orientated crystal. Although the presence of rings rather than discrete peaks is indicative of a range of orientations, for clarity of the following discussion, we will identify the peaks based on the relationship to these two extreme orientational preferences.

We compare the CLs of the most intense diffraction peaks along the q_{xy} and q_z axis, corresponding to the (010) and (001) diffraction, respectively. Both peaks have contributions from all molecular dimensions and provide an overview of the trends in CL upon annealing. Annealing leads to increases in the NDT (010) CL from 11 nm to 20 nm in the neat NDT film and 8 nm to 18 nm in the 40% $PC_{61}BM$ blend films (Table 1). A similar trend is seen in the (001) CL which

increases from 10 nm to 21 nm in the neat and 5 nm to 16 nm in the 40% $PC_{61}BM$ blend films. Despite increases in the CL of (010) and (001) peaks, many other peaks actually show a significant (>50%) decrease in the CL upon annealing (see Tables S2 and S3). The majority of these peaks are associated with end-on oriented domains suggesting that annealing results in a weak preference for side-on oriented domains. Additionally, in the blend film, the $PC_{61}BM$ (311) CL increases slightly from 1.9 to 2.7 nm with annealing. The general increase in CL and the increased number of diffraction peaks observed upon annealing suggest that the annealed film consists of end-on oriented crystallites of NDT, weakly crystalline regions of NDT, and moderately sized crystalline regions of $PC_{61}BM$. Because we are unable to observe disordered domains using X-ray scattering, we can only hypothesize that it is likely that disordered regions of NDT and $PC_{61}BM$ also exist in the thin film, which include those randomly oriented species, such as individual NDT molecules and disordered NDT clusters.

2.2. $PC_{61}BM$ loading and film morphology

The $PC_{61}BM$ loading relative to that of NDT is one way to tune the BHJ film morphology and determine the donor/acceptor ratio for optimal device performance. We chose to survey a broad range of $PC_{61}BM$ loading weight fraction from 0.1 – 80% to map out the film morphology evolution as a function of the $PC_{61}BM$ loading. To determine the specific effect of $PC_{61}BM$ on the NDT crystallite structure and the bulk blend film morphology, we measured the scattering of annealed NDT:$PC_{61}BM$ thin films with 0.1% to 80% w/w $PC_{61}BM$ (Figure 5). Because no observable change in diffraction pattern is observed for BHJ films with 0.1% or 1% $PC_{61}BM$ in comparison to neat NDT films, they are not shown here (see Figure S2). The 30% and 60% $PC_{61}BM$ loadings are also omitted for clarity and may be found in Figure S2. The appearance of

broad peaks at q = 0.7 Å^{-1} and 1.4 Å^{-1} are characteristic of $PC_{61}BM$ domains in the film. They first appear at 20% $PC_{61}BM$ loading and increase in intensity in films with more $PC_{61}BM$, as expected.

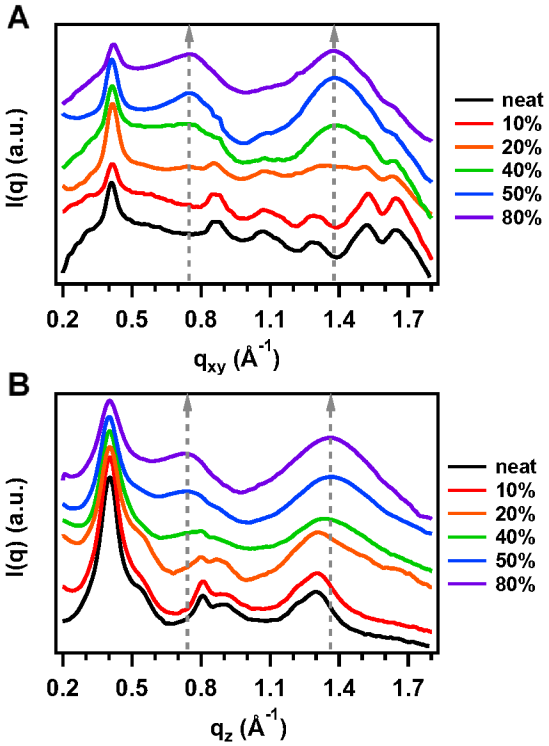

Figure 5. A) In-plane and B) out-of-plane X-ray scattering of neat NDT and select NDT:$PC_{61}BM$ thin films with $PC_{61}BM$ loadings from 0-80%

The scattering intensity of all NDT diffraction peaks decreases with higher $PC_{61}BM$ loading, but the loading at which the scattering signal disappearance occurs varies for each peak. The intensity of peaks $(02\bar{2})$, $(1\bar{1}\bar{2})/(112)$, and $(01\bar{2})$ decreases rapidly and the peaks are no longer present by 30% $PC_{61}BM$ loading (Figure 5). These features roughly correspond to the end-to-end distance between molecules and/or the degree of slip-stacking in the crystal structure. These peaks are also absent in the unannealed neat film scattering suggesting that the slip-stacking intermolecular interaction is weakened. The scattering by peaks $(1\bar{1}\bar{2})$ and (023), corresponding to a mixture of slip-stacking and π-π stacking interactions, is absent at 50% $PC_{61}BM$ loading, while

the $(02\bar{1})$ peak, with a strong lamellar interaction contribution, is last visible in films with 60% $PC_{61}BM$ (Figure 5). The remaining scattering features are still present in films with 80% $PC_{61}BM$ loading. While the high intensity peaks (010) and (001) cannot be clearly attributed to a single intermolecular interaction, the remaining $(02\bar{1})$ peak in the out-of-plane linecut (q = 0.90 Å^{-1}) is clearly associated with the lamellar d-spacing, while the remaining $(1\bar{2}\bar{4})$ peak (q = 1.66 Å^{-1}) is due to the π-π stacking. Peaks (033) and $(02\bar{2})$ (q = 1.53 Å^{-1}and 0.87 Å^{-1}, respectively) also remain, but they are not associated with a single intermolecular interaction. It is important to note that even at very high $PC_{61}BM$ loadings (80%), the NDT still retains both lamellar and π-π stacking interactions in end-on oriented crystals indicating that three-dimensional crystalline NDT regions are still present. It is also possible that side-on NDT crystals are also present, but no π-π stacking interaction is observed for these crystals suggesting that they consist of single sheets dominated by the lamellar intermolecular interaction.

It is possible that the addition of $PC_{61}BM$ to the thin film could result in the formation of a co-crystal or an NDT crystallite intercalated with $PC_{61}BM$. If this were true, we would expect to see an increase in the d-spacing corresponding to each peak dimension. Although no increase is evident at low loadings of $PC_{61}BM$, at 60% $PC_{61}BM$ loading, the (010) and (001) peaks decrease by q = 0.02 Å^{-1}, corresponding to a 1 Å increase in d-spacing for both peaks (Tables S2 and S3). This is indicative of general crystal expansion with very high $PC_{61}BM$ loadings, but does not suggest organized NDT-$PC_{61}BM$ co-crystal formation.

Most of the GIWAXS peaks in BHJ films are rather broad, thus it is difficult to accurately distinguish peak intensities and widths, particularly of the $PC_{61}BM$ (311) and (111) scattering peaks. However, a Scherrer analysis was carried out for the most distinct peaks (001) and (010) as well as the π-π stacking peak $(1\bar{2}\bar{4})$. Interestingly, for $PC_{61}BM$ loading >10%, the CLs of these

peaks do not change much and remain around 13 nm for the (001) and (010) peaks and 3 nm for the $(1\bar{2}\bar{4})$ peaks (Table S2).

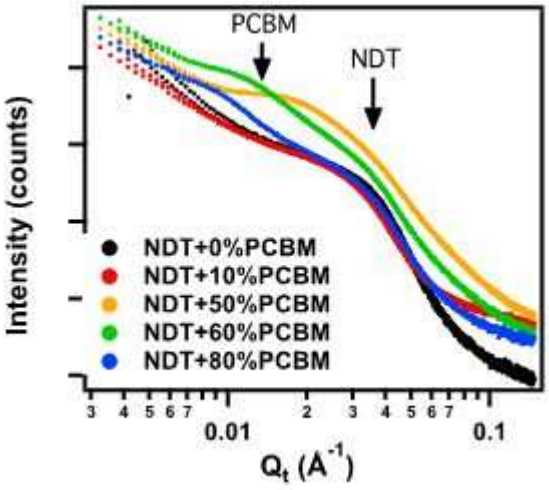

Figure 6. GISAXS scattering patterns of select NDT:$PC_{61}BM$ films with varied $PC_{61}BM$ loadings showing the growth of the $PC_{61}BM$ domains with increasing $PC_{61}BM$ loading.

While the GIWAXS results show the packing of molecules in crystallites as a function of the $PC_{61}BM$ loading, GISAXS signals will determine the domain (e.g., NDT-rich or $PC_{61}BM$-rich) size evolution. Both properties, the crystallinity and the domain size can be directly related to the efficiency of exciton splitting and charge carrier mobility, because the optimized device is always a balance between large donor/acceptor interface in favor of exciton splitting and large domain size for high charge mobility. Figure 6 shows the GISAXS scattering for annealed films of NDT with varying $PC_{61}BM$ loadings. The neat NDT films exhibits a broad scattering feature around q = 0.04 $Å^{-1}$ corresponding to a domain size of ~17 nm, while the CL had an upper bound of ~20 nm from the GIWAXS results. Since GISAXS signals arise from an average of all crystalline orientations in the thin film, the close agreement between these values suggests that the feature in the GISAXS comes from the individual crystallites that give rise to the GIWAXS features. As the $PC_{61}BM$ loading is increased, the NDT-rich domain size only changed slightly ranging from 16 –

19 nm (Figure 6, Table 2). Since the CL of NDT does not change, these domains consist of crystalline NDT regions embedded in less crystalline and/or amorphous NDT-rich domains.

The growth of a new peak around 0.02 $Å^{-1}$ is observed starting at 50% $PC_{61}BM$ loading which corresponds well with the emergence of the $PC_{61}BM$ (311) peak in GIWAXS, and is therefore assigned to the formation of $PC_{61}BM$ domains. As the $PC_{61}BM$ loading is increased, the peak shifts to lower *q* values showing that the $PC_{61}BM$ domains are increasing in size, as expected, with a maximum size of $_{61}$ nm for 80% $PC_{61}BM$ loading. Despite the high $PC_{61}BM$ loading, the NDT domain peak is still observed in the GISAXS scattering pattern.

Table 2. Domain sizes of NDT and $PC_{61}BM$ thin film domains obtained from GISAXS analysis (all films are annealed, and errors for the domain sizes are 1 - 4 nm).

Wt%$PC_{61}BM$	0	10	20	30	40	50	60	80
NDT domain size (nm)	17	19	16	16	16	19	18	18
$PC_{61}BM$ domain size (nm)	NA	NA	NA	NA	NA	34	50	$_{61}$

3. Exciton and charge separation dynamics obtained by transient absorption spectroscopy

One important question is how the film morphology correlates with the exciton and charge separation dynamics that influence OPV performances. As shown above, the film morphology, and in particular, the average $PC_{61}BM$ domain size, varies with the $PC_{61}BM$ concentration, but it is unclear how exciton and charge separation dynamics, as well as device performance would respond to these changes. At one extreme (0.1% loading), each $PC_{61}BM$ molecule is surrounded by NDT molecules and has almost no chance to form $PC_{61}BM$ domains, providing a model system for studying intrinsic exciton splitting and charge separation dynamics. At the other extreme with 80% $PC_{61}BM$ loading, NDT domains or even single molecules are likely to be isolated, which could provide complementary information on the same processes. Accordingly, we tracked

exciton splitting and charge separation dynamics as a function of $PC_{61}BM$ loading using transient absorption (TA) spectroscopy on the femtosecond (fs) to nanosecond (ns) time scale in the near IR (NIR) region, where the exciton (EX), the charge transfer (CT), and the charge separated (CS) states absorb. The CS state is normally detected by the absorption signatures of the acceptor anion or the donor cation, and the NDT cation absorption signal is used to monitor the CS state dynamics in this study. The TA measurements were performed on a dilute NDT solution, neat NDT films (annealed and unannealed), and blend NDT:$PC_{61}BM$ films with $PC_{61}BM$ loading ranging from 0.1-80% as described above. These three sets of data are used to follow intra-donor, inter-donor, and donor-acceptor electronic processes. The exciton spectra and dynamics were first measured for NDT in $CHCl_3$ solution as a reference for optical absorption features for intramolecular exciton species and decay dynamics in this *ada* molecule in the absence of intermolecular interactions. Then annealed and unannealed films of neat NDT and NDT:$PC_{61}BM$ blend films with 40% by weight $PC_{61}BM$ were used to evaluate the impact of NDT crystallinity and NDT:$PC_{61}BM$ interface on exciton dynamics. Based on the results from these measurements, we can establish correlations between the morphology and exciton/charge separation dynamics.

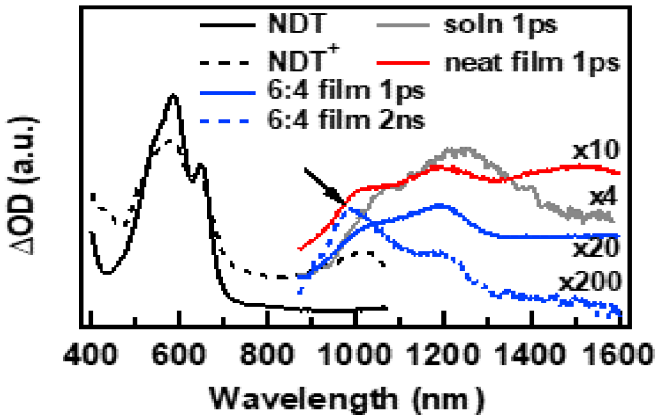

Figure 7. Ground state spectra of NDT and spectral signature of NDT^+ (left side of the panel) and optical transient excited state absorption spectra of NDT solution and NDT neat film at 1 ps, delay and NDT:$PC_{61}BM$ (6:4 w/w) blend film at 1 ps and 2 ns delays (right side of the panel).

The NDT solution in $CHCl_3$ was excited at its absorption maximum of 530 nm (OD = 0.3) in a sealed N_2 environment (Figure S4). The TA spectrum at each pump-probe delay time was fit to multiple Gaussian peaks corresponding to different possible species. The peak amplitudes are extracted as a function of the delay time between the pump and probe laser pulses, from which the kinetics are extracted from multiple exponential fits. The NDT solution spectrum at 1 ps delay (grey solid curve in Figure 7) exhibits a broad absorption peak with a main feature at 1215 nm and a shoulder at 1029 nm. Because both features decay monoexponentially with the same time constant of 850 ps, which is typical for excited states of small organic molecules, thus we assign these features to an EX state localized on a single NDT molecule, or intra-molecular EX state in dilute solution.

The neat NDT film ground state absorption feature (Figure 7 left side) is red-shifted from its solution spectrum,[89] and shows a vibronic structure typical for H-aggregates, with the 0-1 transition at 600 nm greater than the 0-0 transition.[94,95] The TA spectrum of the neat NDT film pumped at 600 nm at a 1-ps delay displays the characteristic EX features as in solution, but the

two spectral features are blue-shifted to 1190 nm and 1020 nm, respectively (Figure 7, red curve), as a result of intermolecular interactions between closely packed molecules. What differs from the solution NDT TA spectrum is a new broad feature emerging around 1500 nm for both the annealed and unannealed NDT films (Figure 7). This feature decays completely in NDT films with two time constants of ~6 ps and ~62 ps for the annealed and ~3 ps and ~52 ps for the unannealed films (Table 3). Since this feature is absent in solution where the excitons are confined within each individual molecules, we attribute it to a charge transfer exciton state with charge density delocalized over two or more energetically distinct NDT molecules due to intermolecular electronic coupling enabled by molecular packing. This inter-NDT CT state is denoted as CT_1.

Table 3. Delocalized charge transfer exciton (CT_1/CT_2) decay dynamics in annealed and unannealed thin films with varying $PC_{61}BM$ loadings (*Indicates unannealed film; ** signal too noisy).

Wt%$PC_{61}BM$	**τ_1 (ps)**	**τ_2 (ps)**	**A_1 (x10^{-3})**	**A_2 (x10^{-3})**
0	5.5 (0.1)	62.0 (1.8)	3.6 (0.04)	1.6 (0.03)
0*	2.7 (0.1)	52.2 (1.0)	7.3 (0.06)	5.6 (0.06)
0.1	7.2 (0.8)	144.6 (24.8)	1.4 (0.07)	0.52 (0.05)
1	4.4 (0.3)	31.7 (2.0)	1.6 (0.05)	0.87 (0.05)
10	5.4 (0.1)	59.7 (1.6)	3.5 (0.03)	1.6 (0.03)
20	4.7 (0.2)	58.0 (3.4)	3.1 (0.07)	1.3 (0.05)
30	3.1 (0.1)	26.1 (1.1)	3.5 (0.06)	2.0 (0.06)
40	1.9 (0.1)	14.7 (0.7)	1.5 (0.02)	0.85 (0.03)
40*	9.3 (0.7)	**	0.75 (0.02)	0.33 (0.01)
50	2.0 (0.2)	20.3 (1.4)	2.1 (0.08)	1.2 (0.05)

60	4.1 (0.2)	77.5 (5.8)	1.4 (0.04)	0.57 (0.03)
80	8.6 (0.4)	1173.2 (90.1)	1.4 (0.03)	0.38 (0.01)

Because of the *ada* arrangement in NDT (Figure 1), the donor and acceptor moieties in one NDT molecule likely interact with the complementary moieties in another NDT molecule in the neat film when they adopt the slipped π-π stacking to form the CT_1 state. This type of species has been previously observed in neat polymer films consisting of domains of variable crystallinity, especially in self-folding conjugated polymer donor materials,[16,96-98] but to our knowledge it has not been characterized experimentally in small molecule films. Since annealing increases the crystallinity of the NDT domains, we expect increased conformational homogeneity and delocalization in the annealed compared to the unannealed films. Indeed, the faster decay rates observed for the unannealed films (Table 3) suggest that the charge transfer state is indeed more localized both spatially and energetically, leading to stronger Coulombic binding and faster geminate recombination decay.

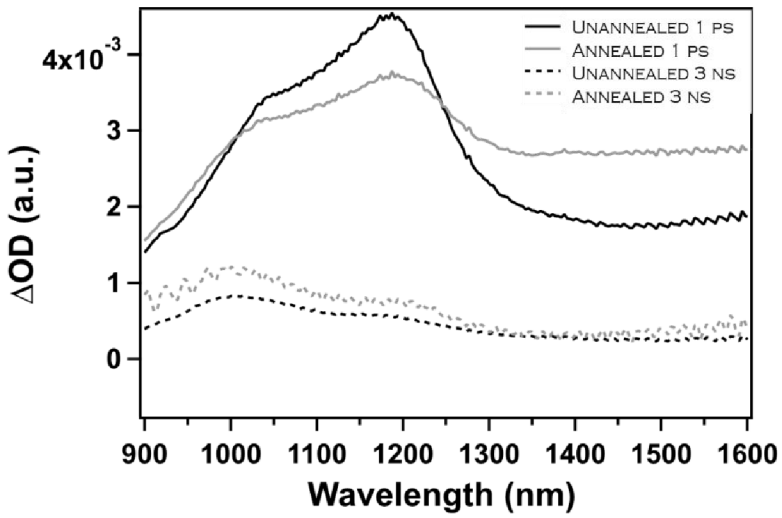

Figure 8. Excited state spectra of unannealed and annealed NDT + 40% $PC_{61}BM$ films at 1 ps and 3 ns delay times normalized by the OD at the excitation wavelength 600 nm. The latter shows peaks around 980 nm assigned as the NDT cation absorption.

Next we examined the BHJ films with 60% NDT + 40% $PC_{61}BM$ (by weight). The main difference in their TA spectra compared to the neat film is the absence of the CT_1 feature at 1500 nm. Unlike the neat NDT film, the TA spectra for the annealed and unannealed blend films display an extremely broad absorption above 1400 nm covering a majority part of the NIR probe spectrum (Figure 8). Because it appears only in the BHJ film and has a totally different shape from the CT_1 state feature at the 1500 nm in the neat NDT film, we assign this broad absorption to a new intermolecular charge transfer state between NDT and $PC_{61}BM$, denoted as CT_2. The relative amplitude of this absorption shelf is significantly higher in the annealed than in the unannealed BHJ films, again indicating the delocalization nature of the charge transfer state. This broad feature decays almost completely on a nanosecond time scale. Compared to the neat film, the decay of the CT_2 state is approximately twice as fast in the unannealed 40% $PC_{61}BM$ film and four times as fast in the annealed 40% $PC_{61}BM$ film (Table 3, Figure 9A). Such differences are related to the CS state generation as discussed below.

It is important to note that unlike the EX decay in NDT in solution, where the same kinetics were detected for the two "EX" features at 1020 and 1190 nm, the corresponding features in the annealed and unannealed BHJ films appear to have significantly different decay kinetics. More importantly, the TA spectra of the two films at a 3-ns delay (when the EX state is mostly gone) show a feature emerging around 980 nm, which coincides with the NDT cation absorption seen in the neat film NDT spectroelectrochemical spectrum with a slight red-shift (Figure 7, dashed black curve). Because of the emergence of this NDT cation peak and its overlap with the 1020 nm feature, the decay of the bluer feature appears to be slower than the redder feature in the BHJ films.

Thus, this 980 nm feature is assigned as the NDT cation, and its kinetics represents the rise and decay of the CS state. The multipeak Gaussian peak fitting reveals the growth of the peak at

980 nm in <1 ps, reaching peak amplitude at 13 ps (Table 4, Figure 10). This cation growth kinetics correspond well to the rapid decay of the EX state (τ_1) and the CT_2 state (τ_2), where τ_1 is shorter in the unannealed film (4.9 ps) than in the annealed film (6.9 ps), and τ_2 is shorter in the annealed film (1.9 ps) than in the unannealed film (9.3 ps). The CT_2 state contributes more to the rise of the CS state in both the annealed and unannealed films (Table 4), and the fast rise from the CS state in the annealed films is indicative of one of its main origins in the CT_2 state. In addition to the longer rise, the unannealed film also exhibits a longer CS lifetime (>3000 ps) than the annealed film (1660 ps). The long lifetime of the CS state may be related to the increased NDT-$PC_{61}BM$ interfacial disorder, which has been shown to reduce the energetic overlap of the NDT and $PC_{61}BM$ states, thereby suppressing bimolecular recombination across the interface.

Table 4. Dynamics of the CS state in unannealed and annealed BHJ thin films with varying $PC_{61}BM$ loadings.

*Indicates unannealed film.

Wt% $PC_{61}BM$	τ_1 (ps) (rise)	τ_2(ps) (rise)	τ_3 (ps)	τ_4 (ps)	A1 ($x10^{-4}$) (rise)	A2 ($x10^{-4}$) (rise)	A3 ($x10^{-4}$)	A4 ($x10^{-4}$)
1	--	--	0.0	875 (103)	--	--	94 (31)	1.5 (0.1)
10	--	--	6.3 (7.3)	1852 (49)	--	--	4.1 (3)	7.2 (0.1)
20	--	--	18.4 (5.6)	>3000	--	--	3.3 (0.7)	8.8 (0.2)
30	--	3.1 (0.1)	294.4 (53.0)	>3000	--	-3.4 (0.5)	3.9 (0.3)	5.8 (0.2)
40	6.9 (0.2)	1.9 (0.0)	--	1660 (58)	-1.3 (0.1)	-2.0 (0.2)	--	2.9 (0.0)
40*	4.9 (0.2)	9.3 (0.7)	--	>3000	-1.7 (0.9)	-3.1 (0.9)	--	4.0 (0.1)
50	--	2.0 (0.2)	--	2175 (128)	--	-4.1 (0.4)	--	4.5 (0.1)
60	--	4.1 (0.2)	--	>3000	--	-3.6 (0.6)	--	3.2 (0.1)
80	--	--	0.2 (0.0)	2066 (89)	--	--	18 (3)	4.4 (0.1)

As the $PC_{61}BM$ loading varies, three different morphology regimes emerge based on the ratio of NDT/$PC_{61}BM$: 1) excess NDT molecules (<30% $PC_{61}BM$), 2) approximately balanced

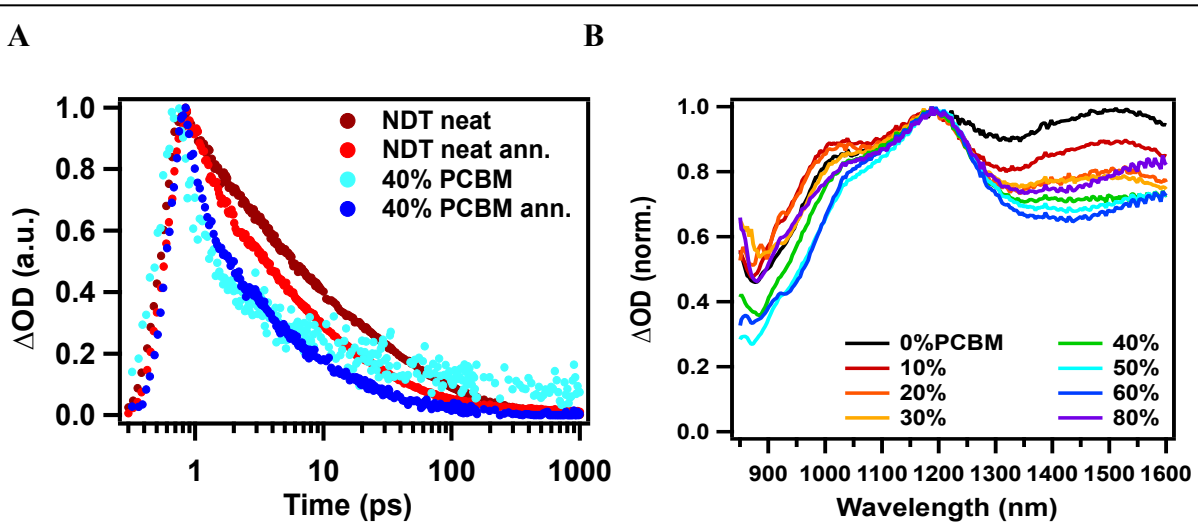

Figure 9. A) Decay of EX in annealed and unannealed neat and NDT+ 40% $PC_{61}BM$ films and B) TA spectra at 1 ps delay for increasing $PC_{61}BM$ loading showing a shift from formation of the polaron state to traditional charge transfer state with increasing $PC_{61}BM$ loading.

numbers of NDT and $PC_{61}BM$ molecules (30% - 60% $PC_{61}BM$), and 3) excess $PC_{61}BM$ molecules (80% $PC_{61}BM$). The exciton dynamics of each of these regimes are characterized by the CS state rise times and the EX, CT_1 and CT_2 state decay(s).

In the regimes where either NDT or $PC_{61}BM$ is present in excess, a <0.25 ps rise time of the CS state is observed, which is comparable to the IRF of 0.24 ps in the experimental setup. The CS state populations in neat NDT and 0.1% $PC_{61}BM$ films are too small to be detected in our experiment. In the 1-20% $PC_{61}BM$ and 80% $PC_{61}BM$ films, the CS state decays with two lifetimes on the order of a few ps and several hundred ps to a few ns, with the majority (>90%) of the CS state population decaying within 10 ps. For the 10% and 20% $PC_{61}BM$ films, an increasing population (~60-70%) of the CS state exhibits the few-ns lifetime. The TA spectra at 1 ps (Figure 9B) show that the CT_1 state (the delocalized charge transfer exciton state among multiple NDT

molecules) is still present as a broad peak centered at 1500 nm in films with excess NDT ($PC_{61}BM$ loading < 30%, Figure 9B). This feature diminishes significantly as the $PC_{61}BM$ loading increases to the middle range (30-60%) and finally shifts to longer wavelengths

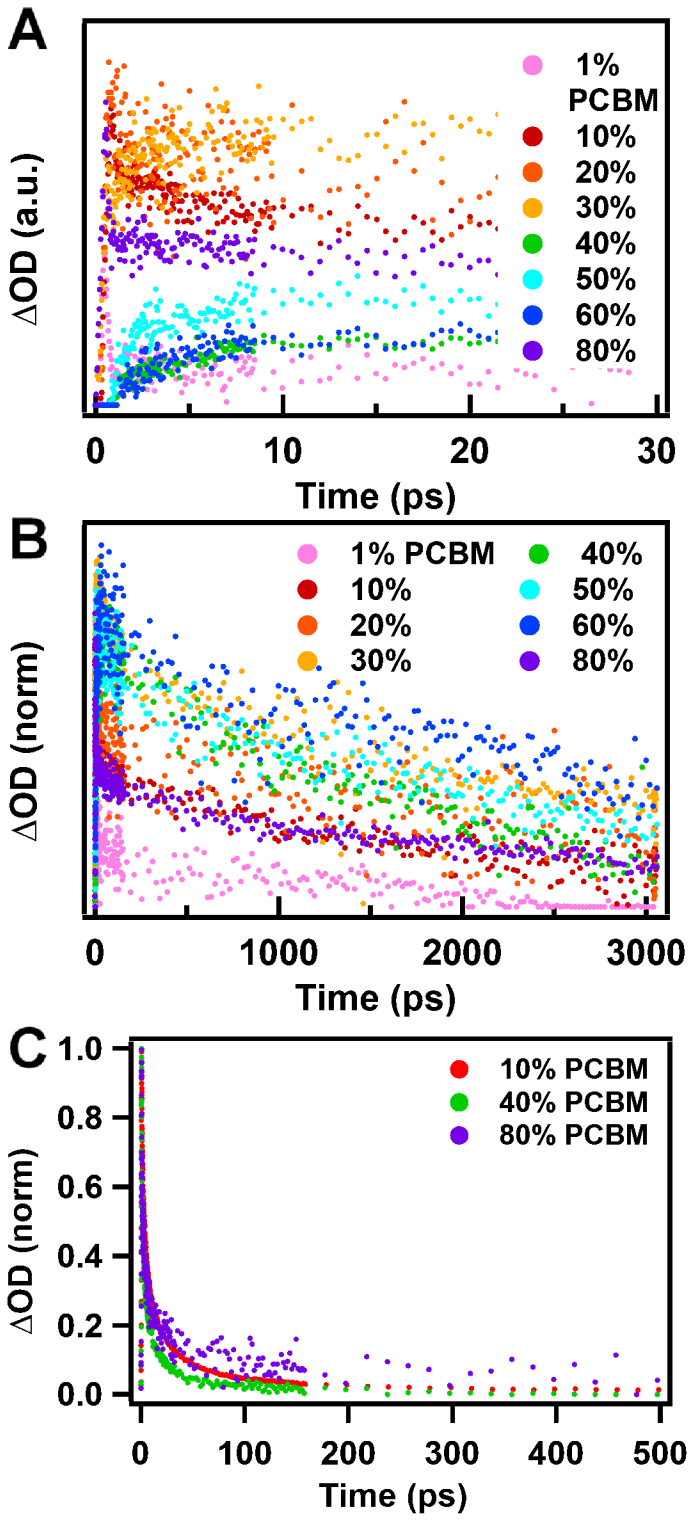

Figure 10. A) Charge generation shown by the rise of the CS state in the first 30 ps delay time window; B) the CS state decay kinetics showing bimolecular recombination rates; C) fast decay kinetics traces of the CT_2 state with different $PC_{61}BM$ loading.

beyond our detection limit (1600 nm) with >60% $PC_{61}BM$, suggesting the formation of the CT_2 state delocalized across the NDT-$PC_{61}BM$ interface as the inter-NDT interactions weaken. Spectra of the 80% $PC_{61}BM$ films also shows this charge transfer state as a pronounced broad peak extending beyond 1600 nm exhibiting two lifetimes, τ_1 ~9 ps (80%) and τ_2 ~1100 ps (20%). This minor component with a long τ_2 lifetime is consistent with significant spatial delocalization in the $PC_{61}BM$ domains which are ~60 nm in the 80% $PC_{61}BM$ film.

When the NDT:$PC_{61}BM$ molar ratio approaches 50:50, we note three changes in the excited state dynamics. First, the rise of the CS state becomes slower (~1-10 ps) and in agreement with the decay time constants of the fast EX and CT_2 states (Figure 10A). While the 40% $PC_{61}BM$ film CS rise exhibits contributions from both the EX and CT_2 states, the other films (30%, 50%, and 60% $PC_{61}BM$) can be fit using a single rise from the CT_2 state. Rise times of 1.9 ps are observed for the 40% and 50% $PC_{61}BM$ films while slower rise times of 3-4 ps are observed in the less balanced blend films (30%, 60% $PC_{61}BM$) (Table 4). Secondly, the CS state exhibits only a single long decay on the order of a few ns for 40 - 60% $PC_{61}BM$ films (Figure 10B), while the 30% $PC_{61}BM$ film exhibits the two decays time constants observed in the excess NDT blend films, albeit with a much longer short time constant (294 ps vs. 18 ps for 20% $PC_{61}BM$). Interestingly, the 40% $PC_{61}BM$ film, which has the highest solar cell performance, also has the shorter decay time of 1659 ± 57 ps, while the 30% $PC_{61}BM$ film has the longest decay time, >3 ns. The third characteristic of these balanced films is a very fast CT2 state decay (Figure 10C), which we attribute to the additional decay pathway of the CT state to the CS state and the presence of a new CT state as observed in the excess $PC_{61}BM$ films. This CT state allows for increased delocalized across the donor-acceptor interface to minimize Coulombic attraction between the hole and electron, thereby increasing the probability and rate of charge separation

4. Device J-V response.

Solar cells of NDT:$PC_{61}BM$ with 0.1-80% $PC_{61}BM$ were also evaluated (Figure 11). Devices of neat NDT resulted in unmeasurable performance and solar cells with 0.1% $PC_{61}BM$ exhibited very low performance (Table 5) limited in all device metrics. However, the addition of 1% $PC_{61}BM$ leads to an increase in V_{oc} attributable to developing aggregation of $PC_{61}BM$, leading to a broadening of the LUMO energetic manifold, allowing increased charge separation.[46] An increase to 10% $PC_{61}BM$ leads to an improved J_{sc} with comparable V_{oc} and *FF*. The J_{sc} is directly correlated with device efficiency (PCE) and peaks at 40% $PC_{61}BM$ loading and then

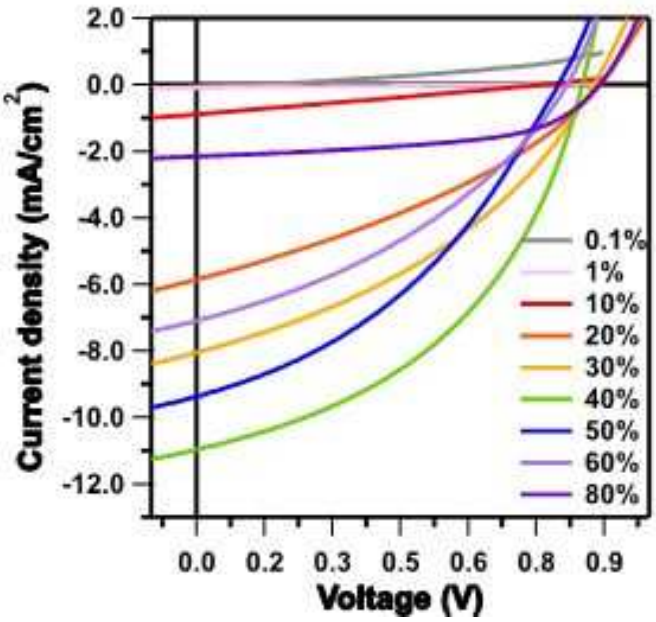

Figure 11. *J-V* curves of NDT:$PC_{61}BM$ solar cells with varying $PC_{61}BM$ loadings

decreases with additional $PC_{61}BM$. V_{oc} exhibits a similar trend, peaking at 20-30% $PC_{61}BM$ and decreasing with additional $PC_{61}BM$. The *FF* increases with $PC_{61}BM$ to 40% $PC_{61}BM$ then decreases before suddenly increasing again with 80% $PC_{61}BM$. This bimodal behavior suggests that although fewer free charges are formed, as evidenced by the low J_{sc} and V_{oc}, more of the charges that are formed, escaped and collected at the appropriate electrode than at lower $PC_{61}BM$ loading. This suggests that 1) most of the free charges exist in crystalline NDT regions close to the

appropriate electrode, and/or 2) despite the lower crystallinity, the NDT domains are still sufficiently crystalline to enable charge transport to the electrodes. Overall, the highest PCE of 4.0% is obtained with 40% $PC_{61}BM$ solar cells.

Table 5. *J-V* OPV device metrics for NDT;$PC_{61}BM$ solar cells with varying $PC_{61}BM$ loadings

Wt% $PC_{61}BM$	V_{oc} (V)	J_{sc} (mA/cm^2)	*FF* (%)	PCE(%)
0.1	0.13	0.06	27.2	0.002
1	0.74	0.089	24.7	0.016
10	0.76	0.89	25.6	0.17
20	0.89	5.9	34.3	1.8
30	0.87	8.2	38.8	2.8
40	0.84	11.2	42.7	4.0
50	0.80	9.5	38.1	2.9
60	0.82	7.1	36.8	2.1
80	0.57	2.1	53.9	0.7

Discussion

One of the challenges in studying organic solar cell systems is understanding how electronic processes correlate with the bulk and interfacial morphology of the active layer. By varying the amount of $PC_{61}BM$ in the films, we are able to vary the degree of order present in the NDT and $PC_{61}BM$ domains and thereby tune the ability of the excited state species to delocalize in the thin film. Ultimately, it is this delocalization that facilitates charge separation, transport, and recombination within the solar cell.

1. *Energy alignment for EX, CT and CS tuned by the molecular environment*

The energy alignment and exciton speciation are important for understanding fundamental electronic processes in small molecular OPV materials. Figure 12 depicts schematically the exciton

state variation in solution, neat NDT and NDT+$PC_{61}BM$ systems in the present study as well as the possible pathways beyond the exciton state. Recall that we have so far encountered three different types of charge transfer excitons that have been denoted as: 1) EX, an isolated exciton within a single NDT molecule; 2) CT_1 a homobimolecular charge transfer exciton when the molecular packing and intermolecular interactions allow; and 3) CT_2, a heterobimolecular charge transfer exciton between NDT and $PC_{61}BM$ domains at the D-A interface. Based on our experimental observations, these three charge transfer exciton states may coexist in the BHJ films and follow different pathways governed by their relative energetics and spatial arrangements in solid films. The EX state, to which we assign the features at 1190 and 1020 nm, still has large populations in both neat and BHJ films at early delay times, while its energetic distribution is narrower than in solution due to increased order. The CT_1 state, to which we assign the broad absorption at 1500 nm, has somewhat higher energy than the EX state, judging by its red-shifted absorption indicating a smaller energy gap to the upper state than from the EX state (assuming the energy of the upper excited state remains approximately the same). If we take 1190 nm and 1500 nm as representative energies for EX and CT_1, respectively, their average energy difference is approximately 0.2 eV. Such an energy shift is likely due to the greater delocalization of the CT_1 state compared to the EX state, as well as the increased energy splitting due to H-aggregated vs. the isolated NDT molecules.

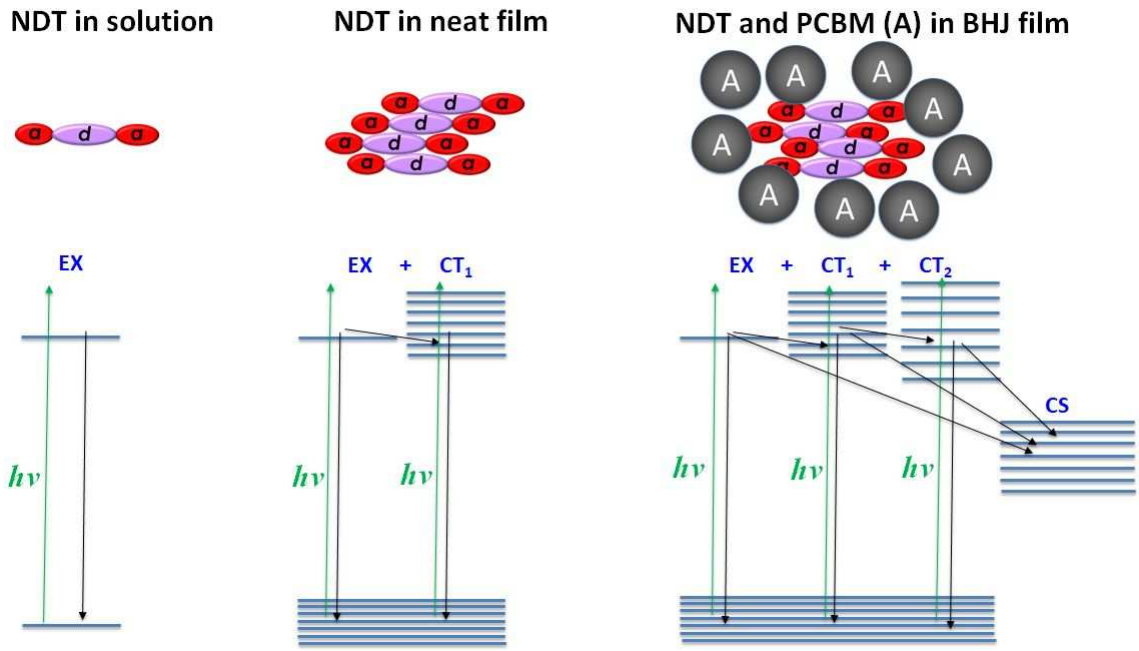

Figure 12. Energetics of three types of excitons in different environments and their possible pathways. The energetic manifolds represent the inhomogeneity of local structures.

As more $PC_{61}BM$ is loaded into the BHJ films, the NDT domains are disrupted, resulting in reduced inter-NDT interactions and increased NDT-$PC_{61}BM$ interactions as the fraction of $PC_{61}BM$ increases. A CT_2 state emerges and becomes clearly observable at high $PC_{61}BM$ loadings, where the CT_1 state converts to the CT_2 state due to the formation of strong interfacial BDT-$PC_{61}BM$ interactions and the concomitant isolation of individual NDT molecules within the $PC_{61}BM$ domains. The excited state absorption of the CT_2 state is further red-shifted to 1600 nm or longer, indicative of its higher energy than the CT_1 state, presumably due to even larger separation of partial charges. In the BHJ films, all three coexisting exciton states have sufficient driving force to reach the CS state, as observed from the correlations between the time constants of the exciton decays and the rise time constants of the cation signal at 980 nm representing the CS state population. However, it is the recombination processes of the hole and electron that determines the loss within the devices and ultimately the device efficiency.

2. Influence of BHJ film morphology on exciton dynamics

In the following sections, we correlate the film morphology tuned by varying the $PC_{61}BM$ loading with the kinetics of the electronic processes relevant to OPV performance in search of the optimal morphology for fast exciton slitting and effective charge carrier transport. To begin, we note that all films exhibit crystallite NDT domains of ~13 nm and π-π stacked domains of ~3 nm, regardless of $PC_{61}BM$ loading. Thus, while the orientation and degree of crystallinity within these domains vary, all films contain at least side-on oriented NDT crystals. The relative loading of

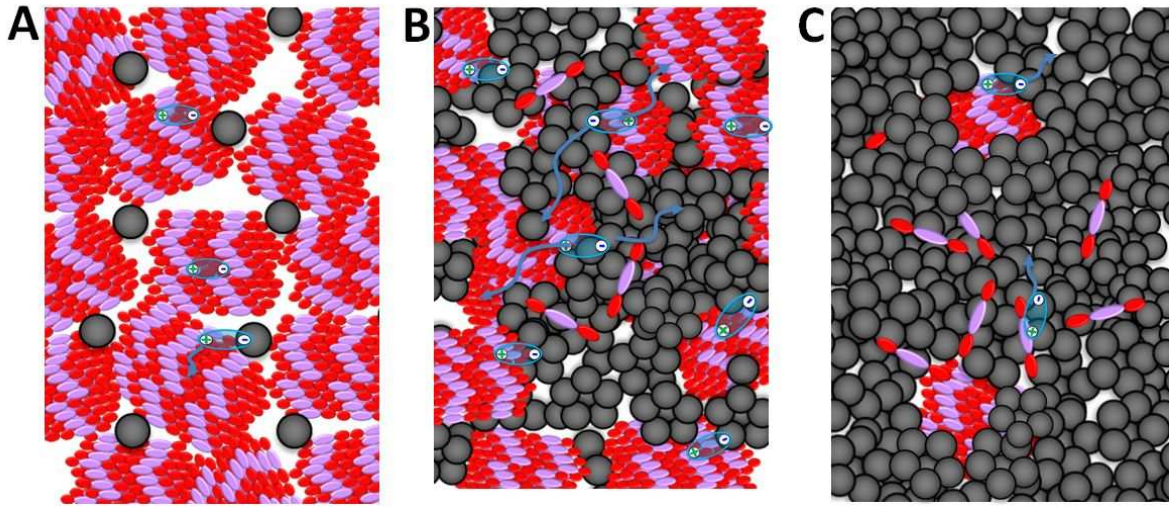

Figure 13. Film morphology evolution as a function of PC61BM loading (see text). A) Regime 1 with the largest NDT domain size and very few isolated PC61BM where discontinuous PC61BM prevents electron diffusion away and the hole will have limited diffusion due to the electrostatic attraction with the electron, leading to charge recombination; B) Regime 2 where NDT:PC61BM is close to 1 and forms bi-continuous pathways for hole and electron diffusion away from where they are separated and the NDT domain size decreases compared to that in Regime 1; C) Regime 3 where PC61BM is much higher in fraction than NDT with decreasing domain size and more isolated NDT molecules, resulting in similar outcome as Regime 1 (see text).

$PC_{61}BM$ can be considered in three regimes in terms of morphology, and their corresponding exciton splitting dynamics are discussed below and schematized in Figure 13.

Regime 1: NDT + <20% loading $PC_{61}BM$ films. In films with low $PC_{61}BM$ loading, the NDT crystallinity is high, comparable to the crystallinity in neat NDT films. The domain sizes measured

by GISAXS are around 16-17 nm with 0 - 20% $PC_{61}BM$ loading, while the crystallite size measured by GIWAXS are around 13 nm, suggesting that each NDT domain is approximately 50% crystalline and consists of a mixture of side-on and end-on oriented domains. No significant $PC_{61}BM$ aggregates are formed, so the $PC_{61}BM$ molecules exist in very small clusters or as single molecules within the NDT domains (Figure 13A).

These films exhibit only an ultrafast rise in the CS state with no contribution to the CS state population originating from the CT_1 state. Although it is clear from the TA spectrum at 1 ps, that the CT_1 state is formed in the thin film, the exciton quickly delocalizes to form either a CT_1 state or a CS state, depending on the proximity of the excitation to a $PC_{61}BM$ molecule. If the excitation occurs within the crystalline NDT domain, a CT_1 state is formed; if, however, the excitation occurs on the edge of an NDT domain in the vicinity of a $PC_{61}BM$ molecule, a CS state is formed. This suggests that a majority of the delocalized CT_1 state may not extend to the edges of the NDT domains (~17 nm) and simply decays quickly (~4 ps) within the NDT domain.

Isolated $PC_{61}BM$ molecules also contribute to the fast decay of the CS state in films with <10% $PC_{61}BM$ loading due to the formation of localized electron species on the $PC_{61}BM$ molecules, which can recombine with the delocalized hole in the crystalline NDT domain. In films with 20% $PC_{61}BM$ loading, the CS state lifetime increases significantly to ~3 ns, suggesting the formation of free charge carriers as $PC_{61}BM$ molecules begin to form continuous electron pathways despite the lack of aggregation.

Regime 2: Films of NDT + 30-60% $PC_{61}BM$ loading. This is an intermediate regime in which the weights of NDT and $PC_{61}BM$ molecules are nearly equal (Figure 13B). $PC_{61}BM$ molecules begin to aggregate at 30% loading, and $PC_{61}BM$ crystals begin to appear at 40% loading, as evidenced by the growth of the $PC_{61}BM$ (111) diffraction peak corresponding to ~7 nm crystallite $PC_{61}BM$

domains. The NDT crystallinity decreases while the CL remains 13 nm, but the NDT domain size from GISAXS decreases to a minimum of 15.5 nm in the NDT + 40% $PC_{61}BM$ film (Figure 13B). In this regime, both NDT and $PC_{61}BM$ crystalline domains of at least 8 nm are present.

In these Regime 2 films, the $CT_{1,2}$ signature is decreased and the CS state signal is increased, suggesting the formation of all three states. Unlike in the Regimes 1 and 3 (see below), the $CT_{1,2}$ states do contribute to the rise of the CS state, and no ultrafast charge separation is seen in films with 30-60% $PC_{61}BM$ loading. Therefore, upon excitation, the exciton does not immediately separate into free charges regardless of the location of the excitation, suggesting that for ultrafast charge generation to occur, a minimum crystallite size must be present for either the NDT or the $PC_{61}BM$. In the case of Regime 1, it is probable that the large NDT domains allow the CT_1 state to access a manifold of energy states, resulting in a higher degree of energetic overlap with the $PC_{61}BM$ molecules. In the case of Regime 3 (see below) with excess PC61BM, aggregated $PC_{61}BM$ domains have been shown to facilitate charge transfer to the degenerate excited state manifold. In comparison, neither the NDT or $PC_{61}BM$ dominate the energetic landscape in Regimes 1 and 3 (below), and the lack of extended energetic overlap of the excited states due to reduced crystallinity (and hence, charge delocalization) results in the initial formation of CT rather than CS species.

Regime 3: Films of excess $PC_{61}BM$ (60-80% $PC_{61}BM$ loading). These films exhibit large $PC_{61}BM$ domains (~60 nm for 80% $PC_{61}BM$ loading) with 7 nm CLs. The overall NDT crystallinity is decreased, but the NDT CL remains 13 nm and the domain size from GISAXS increases to 18 nm, resulting in NDT domains of 38% crystalline regions (Figure 13C).

The combination of crystalline NDT domains and large $PC_{61}BM$ aggregates enables the formation of both delocalized CT_1 and CT_2 species as well as the CS species upon excitation.

However, the relative amounts of NDT and $PC_{61}BM$ favor the formation of the CT_2 species, since excitation of an NDT molecule is more likely to occur near an NDT-$PC_{61}BM$ interface. In neither case do the CT or CS species separate into free charges due to the isolation of the donor or acceptor domains, but free charges are generated on an ultrafast timescale as seen in films with excess NDT. This suggests that if the excitation is close to an NDT-$PC_{61}BM$ interface, the exciton can quickly delocalize into the energetic manifold of the $PC_{61}BM$ domains to form a CS state. If the exciton is generated close to a disordered $PC_{61}BM$ domain, it is possible that the energetics do not allow complete charge separation and lead to the formation of a CT_2 state, while if the excitation occurs within the NDT domain, the exciton will only delocalize into a CT_1 state.

The lifetime of these intermediate species is comparable to those observed in the excess NDT films (Regime 1) with CT state decaying with time constants of ~4 and ~70 ps. Since it is likely that electrons can diffuse rapidly through the $PC_{61}BM$ domains, this suggests that the hole remains trapped near the interface on an energetically and/or spatially isolated NDT molecule. The remaining CS state population has a lifetime of 2000 ps, which is consistent with the hole diffusing into an NDT domain away from an interface. Similar to Regime 1, the excited state delocalization on the $PC_{61}BM$ and the high probability of excited state formation near an NDT-$PC_{61}BM$ interface due to high $PC_{61}BM$ loading results in ultrafast charge generation, but the lack of interconnected NDT domains leads to relatively fast biomolecular recombination as well.

However, unlike in Regimes 1 and 2, these intermediate excited states do contribute to the CS state in Regime 3 through exciton diffusion or delocalization. The slightly reduced size of the NDT domains (15.5 nm vs. 17-18 nm) allows the CT_2 to spatially delocalize to a NDT-$PC_{61}BM$ interface and separate into free charges on the time scale of ~2 ps. This suggests that the CT state dimension in these films is ~7 nm, since growth of the CS state from the CT decay is not observed

in films with larger NDT domains. Similarly, the CS state may be formed when the excitation occurs in a crystalline NDT domain close to an ordered NDT-$PC_{61}BM$ interface, which allows rapid charge separation (~4 ps), but also fast charge recombination (20 ps). This is expected since studies have shown that increased order at the interface leads to faster recombination of charges due to higher degrees of energetic overlap.[6,44,47,72,99] The CT species may also contribute to this fast recombination if it is not sufficiently delocalized at an NDT-$PC_{61}BM$ interface. The CS state shows a lifetime on the order of a few ns, indicating that both the NDT and $PC_{61}BM$ domains form adequately crystalline bicontinuous networks to allow charge transport away from the NDT-$PC_{61}BM$ interface.

3. Effects of annealing the BHJ films

The annealed NDT + 40% $PC_{61}BM$ films exhibit three main differences in morphology from the unannealed: 1) higher crystallinity and larger crystallite regions in NDT domains, 2) reduced amorphous fraction in each NDT domain, and 3) emergence of $PC_{61}BM$ aggregates and crystallites only in the annealed film. The third difference suggests that the $PC_{61}BM$ is distributed throughout the amorphous NDT matrix in the unannealed film and likely primarily disrupts slipped stacked interactions in the NDT crystallite. These isolated $PC_{61}BM$ molecules do not promote delocalization of charges in a $PC_{61}BM$ matrix. The π-π stacking of NDT molecules is maintained in the side-on domains, allowing charge delocalization up to ~8 nm in the unannealed and 13 nm in the annealed films estimated by the CLs of the crystallites.

Both unannealed and annealed BHJ films exhibit similar features in the transient absorption spectra (Figure 8), which are consistent with the coexistence of localized EX state from each NDT molecule featured by absorption peaks around 1020 and 1190 nm, delocalized charge transfer exciton CT_1 within the NDT crystallites featured around 1500 nm (Figure 7) and CT_2 between

NDT crystalline and $PC_{61}BM$ domains featured by a broad absorption above 1400 nm (Figure 8). The presence of the three types of excitons suggests three CS state formation pathways (Figure 12). The first relies on the CT_1 state. Although its characteristic feature at 1500 nm as shown in the neat NDT film (Figure 7, red curve) is buried by the broad absorption of the CT_2 state, the CT_1 state must be present as long as NDT crystallites are present. The broad absorption above 1400 nm in the TA spectrum is likely a combination of the delocalized CT_1 and CT_2 states. The fast decay of the CT_1 state contributes to the rise of the CS state in both films, but the rise is much faster in the annealed film (2 ps) versus the unannealed film (9 ps). This is consistent with a more spatially and energetically delocalized charge transfer exciton in the annealed NDT film, which reduces the energetic barrier for charge separation. In addition, the formation of $PC_{61}BM$ aggregates creates a $PC_{61}BM$ energetic manifold that reduces the energetic barrier across the NDT-$PC_{61}BM$ interface. The second pathway relies on the CT_2 state, the delocalized exciton at the NDT-$PC_{61}BM$ interface, which evolves into the CS state and then separates into free charges (or recombine back to the ground state). Upon the annealing, the initial population of the CT_2 states at 1 ps is higher while the EX state is lower than those of unannealed films, suggesting that more excitons are formed between the NDT and $PC_{61}BM$ while the EX population from energetically isolated NDT molecules is reduced. The exciton contributes to CS state generation in these films with a comparable rate of ~6 ps. The excitons that contribute are likely formed close to a $PC_{61}BM$ molecule or interface and pass quickly through an intermediate species, which we do not observe due to the overlap of the absorption of the CT_1 and CT_2 states. Since the $PC_{61}BM$ is more evenly distributed throughout the unannealed films, it is unsurprising that a larger percentage of excitons contribute to the CS state in the unannealed films than in the annealed film. The third pathway is from the EX state from isolated NDT molecules dispersed in the film, which are not visible from

GIXS results but confirmed by the strong TA signature between 900 and 1300 nm. Upon the annealing, its population is reduced while the populations of the CT_1 and CT_2 states increase. The CS state formation from the EX state is likely short lived unless the bicontinuous channels for the hole and electrons are available.

Both films experience losses from these pathways. In the first pathway, about 1/3 of the CT_1 state decays to the ground state. The CS state lifetime is also much longer in the unannealed film than the annealed film, which can be similarly attributed to increased energetic overlap between the $PC_{61}BM$ energetic manifold and the crystalline NDT energetic manifold in the annealed films, which enable increased charge separation but also faster bimolecular charge recombination.

By comparing these two films, we find that increased NDT crystallinity promotes increased delocalized exciton generation and fast CS state generation from the CT_1 state. This also results in fast geminate and bimolecular recombination due to energetic alignment between NDT molecules and between NDT and $PC_{61}BM$ domains. In contrast, isolated $PC_{61}BM$ molecules in the unannealed NDT film afford slower CS state formation. The formation of these CS states follow three possible pathways with the CS formation time constants on the order of 1-10 ps. Unlike in the films with excess NDT or $PC_{61}BM$, we observe no ultrafast rise of the CS state, suggesting that delocalization close to an interface is vital for this mechanism.

4. Relating morphology and kinetics to solar cell device performance.

The device metrics provide an indication of specific loss mechanisms and confirm the optimization of the morphology at 40% $PC_{61}BM$ loading. All other things being equal, V_{oc} is a measure of bimolecular recombination and is controlled in part by the energetic disorder between the donor and $PC_{61}BM$ molecules. Since energetic disorder is closely linked to the crystallinity, it

is reasonable to attribute the increase in V_{oc} from 0.1% loading to 20-30% loading to an increase in $PC_{61}BM$ aggregation and order. The V_{oc} remains constant for most of the series, only decreasing in the 80% loading film, which can be attributed to an increase in bimolecular recombination due to the formation of small NDT islands and the subsequent short CS state lifetime. The overall V_{oc} are low, suggesting that bimolecular recombination and/or high energetic disorder at the interfaces is limiting the solar cell performance. FF provides another measure of bimolecular recombination, and the generally low FFs in non-inverted small molecule solar cells has been convincingly attributed to poor energetic alignment between the small molecules and the electrodes, which decreases charge collection.[67] In this series, the fill factor is almost universally below 50%, but we have demonstrated increased fill factor in inverted solar cells,[67] indicating that bimolecular recombination at the active layer-electrode interface is a major loss mechanism in these solar cells.

Note that J_{sc} provides insight into the charge generation and monomolecular/geminate recombination processes that dominate at low voltage. We find a wide range of J_{sc} values, which peak at a high J_{sc} = 11.2 mA for 40% $PC_{61}BM$ loading and decreases rapidly for the films with <20% or >60% $PC_{61}BM$ loading. Because the 30-60% $PC_{61}BM$ loading films were the only films to exhibit the growth of the CS state from the CT states, the morphology in this regime maximizes charge generation and/or supresses charge recombination. Low geminate recombination suggests that all the charges formed are able to diffuse away from the NDT-$PC_{61}BM$ interface, indicating sufficient crystalline connectivity between the NDT domains. The $PC_{61}BM$ domains are also sufficiently large (>4 nm crystals) to allow for charge transport and to promote charge separation via delocalization of the CS state into its energetic manifold. In order to allow access to the delocalized CT state while also allowing its recombination, it is essential that the NDT domains contain both amorphous and crystalline regions, as the different energetics of these regions

promote the formation of diffuse polaron states over localized excitons. Overall, we find that a judicious balance of crystallinity and amorphous small molecule domains are necessary for optimized solar cell performance in this system.

Conclusion

In this work, we elucidate the relationship between bulk morphology and charge generation mechanism in a small molecule NDT + $PC_{61}BM$ solar cell. We find that when either the NDT donor molecule or the $PC_{61}BM$ acceptor is in excess by weight, ultrafast charge generation occurs, but the CS state is short lived. On the other hand, when the concentration of NDT and $PC_{61}BM$ is more balanced, charge generation occurs through a delocalized CT state, and the lifetime of the CS state is much prolongedmuch longer on the nanosecond range.

In this system, the CS state lifetime is limited by the physical separation of donor or acceptor domains, resulting in charge trapping islands that foster fast bimolecular recombination. Although the highly crystalline NDT or $PC_{61}BM$ domains in the unbalanced BHJ films facilitates delocalization and fast charge transport, the CS state lifetime also drops to <100 ps, resulting in very low solar cell device performance. This result also reemphasizes the importance of the mutual formation of bicontinuous networks in bulk heterojunction solar cells for efficiency charge transport.

More interestingly, the relative crystallinities of both the NDT and $PC_{61}BM$ components enhance charge generation due to increased orbital overlap at the interfacial region and delocalization of the CT and CS species, but the effect of the amorphous regions is equally important. In fact, the NDT delocalized CT species cannot form unless sufficient crystalline and amorphous regions are present as in the films with low to mid-PC61BM loadings where it

contributes to formation of 60% of the CS state. As the loading is increased, the polaron species dissipates to become a CT species over the NDT-$PC_{61}BM$ interface, where it contributes to the remaining 40% of the free charge generation. Again, without some energetic disorder, delocalization of the CT species in the NDT domains would not be possible and disorder at the interface actually reduces the energetic overlap sufficiently to also reduce bimolecular recombination across the interface.

While it is known that each individual BHJ system will have different optimal morphologies depending on the relative crystallinities of its components and their mutual solubility, we believe that this study provides some general guidelines for future OPV solar cell optimization. First, although mobility is increased in crystalline small molecule regimes, we find that semi-crystalline, three-dimensional crystals of either the donor NDT molecule or the $PC_{61}BM$ provide sufficient mobility for charge extraction, provided that π-π stacking is maintained in the NDT donor domains. In addition, the formation of an amorphous region in the small molecule domains allows for the delocalization of charges, which increases charge generation and decreases the rate of bimolecular recombination. Finally, in order to achieve long CS lifetimes and a delocalized CT state, the $PC_{61}BM$ must have a domain size of at least 4 nm, and more highly crystalline $PC_{61}BM$ domains enable increases in CS lifetimes. We believe that the impact of the amorphous region has been underestimated in small molecule solar cells, and more focus on this region as well as the donor-$PC_{61}BM$ interfacial morphology will provide insights into further optimization of such devices.

Acknowledgements

This research was primarily supported by the Center for Light Energy Activated Redox Processes (LEAP), an Energy Frontier Research Center funded by the U.S. Department of Energy, Office of Science, Office of Basic Energy Sciences, under Award DE-SC0001059. Synthesis and characterization efforts were funded by the U.S. Department of Energy, Office of Science, and Office of Basic Energy Sciences under Award Number DE-FG02-08ER46536. GIXS measurements were carried out at the Beamline 8-IDE of the Advanced Photon Source, Argonne National Laboratory, which is supported by the Director, Office of Science, Office of Basic Energy Sciences, of the U.S. Department of Energy under Contract No. DE-AC02-06CH11357.

Author Contributions

Sylvia Lou, Eric Manley, Joseph Strzalka, Dugan Hayes collected and analyzed X-ray scattering and transient absorption data; Stephen Loser, Kyle Luck, Nanjia Zhou, Matthew Leonardi, and Amod Timalsina designed and synthesized molecules and fabricated/characterized solar cell devices; Mark Hersam, Robert Chang, Tobin Marks and Lin Chen conceptualized and supervised studies; Sylvia Lou, Dugan Hayes, Kyle Luck, Joseph Strzalka, Tobin Marks and Lin Chen composed and refined the manuscript with input from other authors.

References

(1) Few, S.; Frost, J. M.; Nelson, J. Models of charge pair generation in organic solar cells. *Physical Chemistry Chemical Physics* **2015**, *17*, 2311-2325.

(2) Zhu, X. Y.; Monahan, N. R.; Gong, Z. Z.; Zhu, H. M.; Williams, K. W.; Nelson, C. A. Charge Transfer Excitons at van der Waals Interfaces. *Journal of the American Chemical Society* **2015**, *137*, 8313-8320.

(3) Stoltzfus, D. M.; Donaghey, J. E.; Armin, A.; Shaw, P. E.; Burn, P. L.; Meredith, P. Charge Generation Pathways in Organic Solar Cells: Assessing the Contribution from the Electron Acceptor. *Chemical Reviews* **2016**, *116*, 12920-12955.

(4) Gautam, B. R.; Younts, R.; Li, W.; Yan, L.; Danilov, E.; Klump, E.; Constantinou, I.; So, F.; You, W.; Ade, H.; Gundogdu, K. Charge Photogeneration in Organic

Photovoltaics: Role of Hot versus Cold Charge-Transfer Excitons. *Advanced Energy Materials* **2016**, *6*, 1301032-n/a.

(5) Dimitrov, S. D.; Durrant, J. R. Materials Design Considerations for Charge Generation in Organic Solar Cells. *Chem Mater* **2014**, *26*, 616-630.

(6) Bai, R. R.; Zhang, C. R.; Wu, Y. Z.; Yuan, L. H.; Zhang, M. L.; Chen, Y. H.; Liu, Z. J.; Chen, H. S. Interface configuration effects on excitation, exciton dissociation, and charge recombination in organic photovoltaic heterojunction. *International Journal of Quantum Chemistry* **2020**, *120*.

(7) Benatto, L.; Sousa, K. R. D.; Koehler, M. Driving Force for Exciton Dissociation in Organic Solar Cells: The Influence of Donor and Acceptor Relative Orientation. *J Phys Chem C* **2020**, *124*, 13580-13591.

(8) Coropceanu, V.; Chen, X. K.; Wang, T. H.; Zheng, Z. L.; Bredas, J. L. Charge-transfer electronic states in organic solar cells. *Nature Reviews Materials* **2019**, *4*, 689-707.

(9) Li, M. Y.; Yin, H.; Sui, M. Y.; Wang, F.; Liu, Y. H.; Sun, G. Y. In-depth probe of researching interfacial charge transfer process for organic solar cells: A promising bisadduct fullerene derivatives acceptor. *International Journal of Quantum Chemistry* **2019**, *119*.

(10) Ashokan, A.; Wang, T. H.; Coropceanu, V.; Bredas, J. L. Bulk Heterojunction Solar Cells: Insight into Ternary Blends from a Characterization of the Intermolecular Packing and Electronic Properties in the Corresponding Binary Blends. *Advanced Theory and Simulations*.

(11) Kniepert, J.; Lange, I.; van der Kaap, N. J.; Koster, L. J. A.; Neher, D. A Conclusive View on Charge Generation, Recombination, and Extraction in As-Prepared and Annealed P3HT:PCBM Blends: Combined Experimental and Simulation Work. *Advanced Energy Materials* **2014**, *4*, 1301401-n/a.

(12) Zhong, C.; Bartelt, J. A.; McGehee, M. D.; Cao, D.; Huang, F.; Cao, Y.; Heeger, A. J. Influence of Intermixed Donor and Acceptor Domains on the Ultrafast Charge Generation in Bulk Heterojunction Materials. *The Journal of Physical Chemistry C* **2015**, *119*, 26889-26894.

(13) Knupfer, M.; Fink, J.; Fichou, D. Strongly confined polaron excitations in charged organic semiconductors. *Phys Rev B* **2001**, *63*.

(14) Holdcroft, S. A Photochemical Study of Poly(3-Hexylthiophene). *Macromolecules* **1991**, *24*, 4834-4838.

(15) Kaake, L. G.; Jasieniak, J. J.; Bakus, R. C.; Welch, G. C.; Moses, D.; Bazan, G. C.; Heeger, A. J. Photoinduced Charge Generation in a Molecular Bulk Heterojunction Material. *Journal of the American Chemical Society* **2012**, *134*, 19828-19838.

(16) Rolczynski, B. S.; Szarko, J. M.; Son, H. J.; Liang, Y.; Yu, L.; Chen, L. X. Ultrafast Intramolecular Exciton Splitting Dynamics in Isolated Low-Band-Gap Polymers and Their Implications in Photovoltaic Materials Design. *Journal of the American Chemical Society* **2012**, *134*, 4142-4152.

(17) Di Nuzzo, D.; Viola, D.; Fischer, F. S. U.; Cerullo, G.; Ludwigs, S.; Da Como, E. Enhanced Photogeneration of Polaron Pairs in Neat Semicrystalline Donor–Acceptor Copolymer Films via Direct Excitation of Interchain Aggregates. *The Journal of Physical Chemistry Letters* **2015**, *6*, 1196-1203.

(18) De Sio, A.; Troiani, F.; Maiuri, M.; Rehault, J.; Sommer, E.; Lim, J.; Huelga, S. F.; Plenio, M. B.; Rozzi, C. A.; Cerullo, G.; Molinari, E.; Lienau, C. Tracking the coherent generation of polaron pairs in conjugated polymers. *Nat Commun* **2016**, *7*.

(19) Devizis, A.; De Jonghe-Risse, J.; Hany, R.; Nuesch, F.; Jenatsch, S.; Gulbinas, V.; Moser, J. E. Dissociation of Charge Transfer States and Carrier Separation in Bilayer Organic Solar Cells: A Time-Resolved Electroabsorption Spectroscopy Study. *Journal of the American Chemical Society* **2015**, *137*, 8192-8198.

(20) Yao, H. F.; Cui, Y.; Qian, D. P.; Ponseca, C. S.; Honarfar, A.; Xu, Y.; Xin, J. M.; Chen, Z. Y.; Hong, L.; Gao, B. W.; Yu, R. N.; Zu, Y. F.; Ma, W.; Chabera, P.; Pullerits, T.; Yartsev, A.; Gao, F.; Hou, J. H. 14.7% Efficiency Organic Photovoltaic Cells Enabled by Active Materials with a Large Electrostatic Potential Difference. *Journal of the American Chemical Society* **2019**, *141*, 7743-7750.

(21) Shimazaki, T.; Nakajima, T. Theoretical Study on Hot Charge-Transfer States and Dimensional Effects of Organic Photocells based on the Ideal Diode Model. *Physical Chemistry Chemical Physics* **2017**.

(22) Kaake, L. G.; Welch, G. C.; Moses, D.; Bazan, G. C.; Heeger, A. J. Influence of Processing Additives on Charge-Transfer Time Scales and Sound Velocity in Organic Bulk Heterojunction Films. *J. Phys. Chem. Lett.* **2012**, *3*, 1253-1257.

(23) Fazzi, D.; Barbatti, M.; Thiel, W. Unveiling the Role of Hot Charge-Transfer States in Molecular Aggregates via Nonadiabatic Dynamics. *Journal of the American Chemical Society* **2016**, *138*, 4502-4511.

(24) Vandewal, K.; Himmelberger, S.; Salleo, A. Structural Factors That Affect the Performance of Organic Bulk Heterojunction Solar Cells. *Macromolecules* **2013**, *46*, 6379-6387.

(25) Laquai, F.; Andrienko, D.; Deibel, C.; Neher, D.: Charge Carrier Generation, Recombination, and Extraction in Polymer-Fullerene Bulk Heterojunction Organic Solar Cells. In *Elementary Processes in Organic Photovoltaics*; Leo, K., Ed.; Advances in Polymer Science 272; Springer International Publishing, 2017; pp 267-291.

(26) Fauvell, T. J.; Cai, Z.; Kirschner, M. S.; Helweh, W.; Kim, P.; Zheng, T.; Yu, L.; Chen, L. X. Effects of Intra- and Interchain Interactions on Exciton Dynamics of PTB7 Revealed by Model Oligomers. *Molecules* **2020**, *25*, 2441-2453.

(27) Fauvell, T. J.; Zheng, T.; Jackson, N. E.; Ratner, M. A.; Yu, L.; Chen, L. X. Photophysical and Morphological Implications of Single-Strand Conjugated Polymer Folding in Solution. *Chemistry of Materials* **2016**, *28*, 2814-2822.

(28) Che, Y. X.; Zhang, Y. L.; Yang, Y. L.; Liu, C. H.; Izquierdo, R.; Xiao, S. S.; Perepichka, D. F. Understanding the Photovoltaic Behavior of A-D-A Molecular Semiconductors through a Permutation of End Groups. *Journal of Organic Chemistry* **2020**, *85*, 52-61.

(29) Shaw, P. E.; Ruseckas, A.; Samuel, I. D. W. Exciton Diffusion Measurements in Poly(3-hexylthiophene). *Advanced Materials* **2008**, *20*, 3516-3520.

(30) Proctor, C. M.; Love, J. A.; Nguyen, T. Q. Mobility Guidelines for High Fill Factor Solution-Processed Small Molecule Solar Cells. *Advanced Materials* **2014**, *26*, 5957-+.

(31) Li, W. T.; Abrecht, S.; Yang, L. Q.; Roland, S.; Tumbleston, J. R.; McAfee, T.; Yan, L.; Kelly, M. A.; Ade, H.; Neher, D.; You, W. Mobility-Controlled Performance of Thick Solar Cells Based on Fluorinated Copolymers. *Journal of the American Chemical Society* **2014**, *136*, 15566-15576.

(32) Chen, W.; Xu, T.; He, F.; Wang, W.; Wang, C.; Strzalka, J.; Liu, Y.; Wen, J.; Miller, D. J.; Chen, J.; Hong, K.; Yu, L.; Darling, S. B.; Hong, O. K.; Yu, O. L. Hierarchical nanomorphologies promote exciton dissociation in polymer/fullerene bulk heterojunction solar cells. *Nano letters* **2011**, *11*, 3707.

(33) Maturova, K.; van Bavel, S. S.; Wienk, M. M.; Janssen, R. A. J.; Kemerink, M. Description of the Morphology Dependent Charge Transport and Performance of Polymer:Fullerene Bulk Heterojunction Solar Cells. *Adv Funct Mater* **2011**, *21*, 261-269.

(34) Hedley, G. J.; Ward, A. J.; Alekseev, A.; Howells, C. T.; Martins, E. R.; Serrano, L. A.; Cooke, G.; Ruseckas, A.; Samuel, I. D. W. Determining the optimum morphology in high-performance polymer-fullerene organic photovoltaic cells. *Nat Commun* **2013**, *4*.

(35) Lee, H.; Park, C.; Sin, D. H.; Park, J. H.; Cho, K. Recent Advances in Morphology Optimization for Organic Photovoltaics. *Advanced Materials* **2018**, *30*.

(36) Sini, G. J.; Schubert, M.; Risko, C.; Roland, S.; Lee, O. P.; Chen, Z. H.; Richter, T. V.; Dolfen, D.; Coropceanu, V.; Ludwigs, S.; Scherf, U.; Facchetti, A.; Frechet, J. M. J.; Neher, D. On the Molecular Origin of Charge Separation at the Donor-Acceptor Interface. *Advanced Energy Materials* **2018**, *8*.

(37) Tamai, Y.; Ohkita, H.; Benten, H.; Ito, S. Exciton Diffusion in Conjugated Polymers: From Fundamental Understanding to Improvement in Photovoltaic Conversion Efficiency. *The Journal of Physical Chemistry Letters* **2015**, *6*, 3417-3428.

(38) Reid, O. G.; Pensack, R. D.; Song, Y.; Scholes, G. D.; Rumbles, G. Charge Photogeneration in Neat Conjugated Polymers. *Chem Mater* **2014**, *26*, 561-575.

(39) Szarko, J. M.; Rolczynski, B. S.; Lou, S. J.; Xu, T.; Strzalka, J.; Marks, T. J.; Yu, L. P.; Chen, L. X. Photovoltaic Function and Exciton/Charge Transfer Dynamics in a Highly Efficient Semiconducting Copolymer. *Adv Funct Mater* **2014**, *24*, 10-26.

(40) Rolczynski, B. S.; Szarko, J. M.; Son, H. J.; Yu, L.; Chen, L. X. Effects of Exciton Polarity in Charge-Transfer Polymer/PCBM Bulk Heterojunction Films. *J. Phys. Chem. Lett.* **2014**, *5*, 1856−1863.

(41) Xie, Y.; Zheng, J.; Lan, Z. G. Full-dimensional multilayer multiconfigurational time-dependent Hartree study of electron transfer dynamics in the anthracene/C60 complex. *Journal of Chemical Physics* **2015**, *142*.

(42) Candiotto, G.; Torres, A.; Mazon, K. T.; Rego, L. G. C. Charge Generation in Organic Solar Cells: Interplay of Quantum Dynamics, Decoherence, and Recombination. *J Phys Chem C* **2017**, *121*, 23276-23286.

(43) Gelinas, S.; Rao, A.; Kumar, A.; Smith, S. L.; Chin, A. W.; Clark, J.; van der Poll, T. S.; Bazan, G. C.; Friend, R. H. Ultrafast Long-Range Charge Separation in Organic Semiconductor Photovoltaic Diodes. *Science* **2014**, *343*, 512-516.

(44) Kelley, A.; Patel, K.; Bittner, E. R. Quantum Simulations of Charge Separation at a Model Donor-Acceptor Interface: Role of Delocalization and Local Packing. *Advances in Condensed Matter Physics* **2018**, *2018*.

(45) Lee, M. H.; Arago, J.; Troisi, A. Charge Dynamics in Organic Photovoltaic Materials: Interplay between Quantum Diffusion and Quantum Relaxation. *J Phys Chem C* **2015**, *119*, 14989-14998.

(46) Savoie, B. M.; Rao, A.; Bakulin, A. A.; Gelinas, S.; Movaghar, B.; Friend, R. H.; Marks, T. J.; Ratner, M. A. Unequal Partnership: Asymmetric Roles of Polymeric Donor and Fullerene Acceptor in Generating Free Charge. *Journal of the American Chemical Society* **2014**, *136*, 2876-2884.

(47) Jailaubekov, A. E.; Willard, A. P.; Tritsch, J. R.; Chan, W. L.; Sai, N.; Gearba, R.; Kaake, L. G.; Williams, K. J.; Leung, K.; Rossky, P. J.; Zhu, X. Y. Hot charge-transfer excitons set the time limit for charge separation at donor/acceptor interfaces in organic photovoltaics. *Nat Mater* **2013**, *12*, 66-73.

(48) Caruso, D.; Troisi, A. Long-range exciton dissociation in organic solar cells. *Proceedings of the National Academy of Sciences of the United States of America* **2012**, *109*, 13498-13502.

(49) Bakulin, A. A.; Rao, A.; Pavelyev, V. G.; Van Loosdrecht, P. H. M.; Pshenichnikov, M. S.; Niedzialek, D.; Cornil, J.; Beljonne, D.; Friend, R. H. The role of driving energy and delocalized States for charge separation in organic semiconductors. *Science* **2012**, *335*, 1340-1344.

(50) Sweetnam, S.; Graham, K. R.; Ngongang Ndjawa, G. O.; Heumüller, T.; Bartelt, J. A.; Burke, T. M.; Li, W.; You, W.; Amassian, A.; McGehee, M. D. Characterization of the Polymer Energy Landscape in Polymer:Fullerene Bulk Heterojunctions with Pure and Mixed Phases. *Journal of the American Chemical Society* **2014**, *136*, 14078-14088.

(51) Paquin, F.; Latini, G.; Sakowicz, M.; Karsenti, P. L.; Wang, L. J.; Beljonne, D.; Stingelin, N.; Silva, C. Charge Separation in Semicrystalline Polymeric Semiconductors by Photoexcitation: Is the Mechanism Intrinsic or Extrinsic? *Phys Rev Lett* **2011**, *106*.

(52) Shoaee, S.; Subramaniyan, S.; Xin, H.; Keiderling, C.; Tuladhar, P. S.; Jamieson, F.; Jenekhe, S. A.; Durrant, J. R. Charge Photogeneration for a Series of Thiazolo-Thiazole Donor Polymers Blended with the Fullerene Electron Acceptors PCBM and ICBA. *Adv Funct Mater* **2013**, *23*, 3286-3298.

(53) Ma, H. B.; Troisi, A. Direct Optical Generation of Long-Range Charge-Transfer States in Organic Photovoltaics. *Advanced Materials* **2014**, *26*, 6163-+.

(54) Shen, X.; Han, G.; Yi, Y. The nature of excited states in dipolar donor/fullerene complexes for organic solar cells: evolution with the donor stack size. *Physical Chemistry Chemical Physics* **2016**, *18*, 15955-15963.

(55) Chen, C. H.; Ting, H. C.; Li, Y. Z.; Lo, Y. C.; Sher, P. H.; Wang, J. K.; Chiu, T. L.; Lin, C. F.; Hsu, I. S.; Lee, J. H.; Liu, S. W.; Wong, K. T. New D-A-A-Configured Small-Molecule Donors for High-Efficiency Vacuum-Processed Organic Photovoltaics under Ambient Light. *Acs Applied Materials & Interfaces* **2019**, *11*, 8337-8349.

(56) Sharenko, A.; Gehrig, D.; Laquai, F.; Nguyen, T.-Q. The Effect of Solvent Additive on the Charge Generation and Photovoltaic Performance of a Solution-Processed Small Molecule:Perylene Diimide Bulk Heterojunction Solar Cell. *Chem Mater* **2014**, *26*, 4109-4118.

(57) Petrus, M. L.; Morgenstern, F. S. F.; Sadhanala, A.; Friend, R. H.; Greenham, N. C.; Dingemans, T. J. Device Performance of Small-Molecule Azomethine-Based Bulk Heterojunction Solar Cells. *Chem Mater* **2015**, *27*, 2990-2997.

(58) Hartnett, P. E.; Dyar, S. M.; Margulies, E. A.; Shoer, L. E.; Cook, A. W.; Eaton, S. W.; Marks, T. J.; Wasielewski, M. R. Long-lived charge carrier generation in ordered films of a covalent perylenediimide-diketopyrrolopyrrole-perylenediimide molecule. *Chem Sci* **2015**, *6*, 402-411.

(59) Mukherjee, S.; Proctor, C. M.; Bazan, G. C.; Nguyen, T. Q.; Ade, H. Significance of Average Domain Purity and Mixed Domains on the Photovoltaic Performance of High-Efficiency Solution-Processed Small-Molecule BHJ Solar Cells. *Advanced Energy Materials* **2015**, *5*, 1500877.

(60) Paudel, K.; Johnson, B.; Thieme, M.; Haley, M. M.; Payne, M. M.; Anthony, J. E.; Ostroverkhova, O. Enhanced charge photogeneration promoted by crystallinity in small-molecule donor-acceptor bulk heterojunctions. *Applied Physics Letters* **2014**, *105*.

(61) Bernardo, B.; Cheyns, D.; Verreet, B.; Schaller, R. D.; Rand, B. P.; Giebink, N. C. Delocalization and dielectric screening of charge transfer states in organic photovoltaic cells. *Nat Commun* **2014**, *5*.

(62) D'Avino, G.; Olivier, Y.; Muccioli, L.; Beljonne, D. Do charges delocalize over multiple molecules in fullerene derivatives? *Journal of Materials Chemistry C* **2016**, *4*, 3747-3756.

(63) Mukherjee, S.; Jiao, X.; Ade, H. Charge Creation and Recombination in Multi-Length Scale Polymer:Fullerene BHJ Solar Cell Morphologies. *Advanced Energy Materials* **2016**, *6*, 1600699.

(64) Tamai, Y.; Tsuda, K.; Ohkita, H.; Benten, H.; Ito, S. Charge-carrier generation in organic solar cells using crystalline donor polymers. *Physical Chemistry Chemical Physics* **2014**, *16*, 20338-20346.

(65) Son, S. Y.; Kim, Y.; Lee, J.; Lee, G.-Y.; Park, W.-T.; Noh, Y.-Y.; Park, C. E.; Park, T. High-Field-Effect Mobility of Low-Crystallinity Conjugated Polymers with Localized Aggregates. *Journal of the American Chemical Society* **2016**, *138*, 8096-8103.

(66) Lou, S. J.; Zhou, N. J.; Guo, X. G.; Chang, R. P. H.; Marks, T. J.; Chen, L. X. Effects of 1,8-diiodooctane on domain nanostructure and charge separation dynamics in PC71BM-based bulk heterojunction solar cells. *Journal of Materials Chemistry A* **2018**, *6*, 23805-23818.

(67) Loser, S.; Valle, B.; Luck, K. A.; Song, C. K.; Ogien, G.; Hersam, M. C.; Singer, K. D.; Marks, T. J. High-Efficiency Inverted Polymer Photovoltaics via Spectrally Tuned Absorption Enhancement. *Advanced Energy Materials* **2014**, *4*.

(68) Few, S.; Frost, J. M.; Kirkpatrick, J.; Nelson, J. Influence of Chemical Structure on the Charge Transfer State Spectrum of a Polymer:Fullerene Complex. *The Journal of Physical Chemistry C* **2014**, *118*, 8253-8261.

(69) Wilcox, D. E.; Lee, M. H.; Sykes, M. E.; Niedringhaus, A.; Geva, E.; Dunietz, B. D.; Shtein, M.; Ogilvie, J. P. Ultrafast Charge-Transfer Dynamics at the Boron Subphthalocyanine Chloride/C-60 Heterojunction: Comparison between Experiment and Theory. *J. Phys. Chem. Lett.* **2015**, *6*, 569-575.

(70) Liu, T.; Cheung, D. L.; Troisi, A. Structural variability and dynamics of the P3HT/PCBM interface and its effects on the electronic structure and the charge-transfer rates in solar cells. *Physical Chemistry Chemical Physics* **2011**, *13*, 21461-21470.

(71) Akaike, K.; Kumai, T.; Nakano, K.; Abdullah, S.; Ouchi, S.; Uemura, Y.; Ito, Y.; Onishi, A.; Yoshida, H.; Tajima, K.; Kanai, K. Effects of Molecular Orientation of a Fullerene Derivative at the Donor/Acceptor Interface on the Device Performance of Organic Photovoltaics. *Chem Mater* **2018**, *30*, 8233-8243.

(72) Akaike, K.; Onishi, A.; Wakayama, Y.; Kanai, K. Structural Disordering upon Formation of Molecular Heterointerfaces. *J Phys Chem C* **2019**, *123*, 12242-12248.

(73) Shen, X. X.; Han, G. C.; Yi, Y. P. The nature of excited states in dipolar donor/fullerene complexes for organic solar cells: evolution with the donor stack size. *Physical Chemistry Chemical Physics* **2016**, *18*, 15955-15963.

(74) Yost, S. R.; Van Voorhis, T. Electrostatic Effects at Organic Semiconductor Interfaces: A Mechanism for "Cold" Exciton Breakup. *J Phys Chem C* **2013**, *117*, 5617-5625.

(75) Isaacs, E. B.; Sharifzadeh, S.; Ma, B. W.; Neaton, J. B. Relating Trends in First-Principles Electronic Structure and Open-Circuit Voltage in Organic Photovoltaics. *J. Phys. Chem. Lett.* **2011**, *2*, 2531-2537.

(76) Chen, H. P.; Peet, J.; Hu, S.; Azoulay, J.; Bazan, G.; Dadmun, M. The Role of Fullerene Mixing Behavior in the Performance of Organic Photovoltaics: PCBM in Low-Bandgap Polymers. *Adv Funct Mater* **2014**, *24*, 140-150.

(77) Ma, H. B.; Troisi, A. Modulating the Exciton Dissociation Rate by up to More than Two Orders of Magnitude by Controlling the Alignment of LUMO+1 in Organic Photovoltaics. *J Phys Chem C* **2014**, *118*, 27272-27280.

(78) Bittner, E. R.: Competing role of quantum localization and interfacial disorder in determining triplet exciton fission and recombination dynamics in polymer/fullerene photovoltaics. In *Physical Chemistry of Interfaces and Nanomaterials Xiii*; Banerji, N., Hayes, S. C., Silva, C., Eds.; Proceedings of SPIE; Spie-Int Soc Optical Engineering: Bellingham, 2014; Vol. 9165.

(79) Bittner, E. R.; Silva, C. Noise-induced quantum coherence drives photo-carrier generation dynamics at polymeric semiconductor heterojunctions. *Nat Commun* **2014**, *5*.

(80) Mukherjee, S.; Jiao, X. C.; Ade, H. Charge Creation and Recombination in Multi-Length Scale Polymer:Fullerene BHJ Solar Cell Morphologies. *Advanced Energy Materials* **2016**, *6*.

(81) Osaka, M.; Benten, H.; Ohkita, H.; Ito, S. Intermixed Donor/Acceptor Region in Conjugated Polymer Blends Visualized by Conductive Atomic Force Microscopy. *Macromolecules* **2017**, *50*, 1618-1625.

(82) Knall, A.-C.; Ashraf, R. S.; Nikolka, M.; Nielsen, C. B.; Purushothaman, B.; Sadhanala, A.; Hurhangee, M.; Broch, K.; Harkin, D. J.; Novák, J.; Neophytou, M.; Hayoz, P.; Sirringhaus, H.; McCulloch, I. Naphthacenodithiophene Based Polymers—New Members of the Acenodithiophene Family Exhibiting High Mobility and Power Conversion Efficiency. *Adv Funct Mater* **2016**, *26*, 6961-6969.

(83) Bartelt, J. A.; Beiley, Z. M.; Hoke, E. T.; Mateker, W. R.; Douglas, J. D.; Collins, B. A.; Tumbleston, J. R.; Graham, K. R.; Amassian, A.; Ade, H.; Frechet, J. M. J.; Toney, M. F.; McGehee, M. D. The Importance of Fullerene Percolation in the Mixed Regions of Polymer-Fullerene Bulk Heterojunction Solar Cells. *Advanced Energy Materials* **2013**, *3*, 364-374.

(84) Kyaw, A. K. K.; Wang, D. H.; Luo, C.; Cao, Y.; Nguyen, T.-Q.; Bazan, G. C.; Heeger, A. J. Effects of Solvent Additives on Morphology, Charge Generation, Transport, and Recombination in Solution-Processed Small-Molecule Solar Cells. *Advanced Energy Materials* **2014**, *4*, 1301469-n/a.

(85) Proctor, C. M.; Kim, C.; Neher, D.; Nguyen, T.-Q. Nongeminate Recombination and Charge Transport Limitations in Diketopyrrolopyrrole-Based Solution-Processed Small Molecule Solar Cells. *Adv Funct Mater* **2013**, n/a-n/a.

(86) Londi, G.; Dilmurat, R.; D'Avino, G.; Lemaur, V.; Olivier, Y.; Beljonne, D. Comprehensive modelling study of singlet exciton diffusion in donor-acceptor dyads: when small changes in chemical structure matter. *Physical Chemistry Chemical Physics* **2019**, *21*, 25023-25034.

(87) Loser, S.; Bruns, C. J.; Miyauchi, H.; Ortiz, R. P.; Facchetti, A.; Stupp, S. I.; Marks, T. J. A Naphthodithiophene-Diketopyrrolopyrrole Donor Molecule for Efficient Solution-Processed Solar Cells. *Journal of the American Chemical Society* **2011**, *133*, 8142-8145.

(88) Riano, A.; Arrechea-Marcos, I.; Mancheno, M. J.; Burrezo, P. M.; de la Pena, A.; Loser, S.; Timalsina, A.; Facchetti, A.; Marks, T. J.; Casado, J.; Navarrete, J. T. L.; Ortiz, R. P.; Segura, J. L. Benzotrithiophene versus Benzo/Naphthodithiophene Building Blocks: The Effect

of Star-Shaped versus Linear Conjugation on Their Electronic Structures. *Chem-Eur J* **2016**, *22*, 6374-6381.

(89) Loser, S.; Lou, S. J.; Savoie, B. M.; Bruns, C. J.; Timalsina, A.; Leonardi, M. J.; Smith, J.; Harschneck, T.; Turrisi, R.; Zhou, N.; Stern, C. L.; Sarjeant, A. A.; Facchetti, A.; Chang, R. P. H.; Stupp, S. I.; Ratner, M. A.; Chen, L. X.; Marks, T. J. Systematic evaluation of structure-property relationships in heteroacene - diketopyrrolopyrrole molecular donors for organic solar cells. *Journal of Materials Chemistry A* **2017**.

(90) Jiang, Z.; Li, X.; Strzalka, J.; Sprung, M.; Sun, T.; Sandy, A. R.; Narayanan, S.; Lee, D. R.; Wang, J. The dedicated high-resolution grazing-incidence X-ray scattering beamline 8-ID-E at the Advanced Photon Source *J. Synchrotron Rad.* **2012**, *19*, 627 - 636.

(91) Jiang, Z. GIXSGUI: a MATLAB toolbox for grazing-incidence X-ray scattering data visualization and reduction, and indexing of buried three-dimensional periodic nanostructured films. *J. Appl. Cryst.* **2015**, *48*, 917-926.

(92) Smilgies, D.-M. Scherrer grain-size analysis adapted to grazingincidence scattering with area detectors. *J. Appl. Cryst.* **2009**, *42*, 1030–1034.

(93) Youn, J.; Huang, P.-Y.; Huang, Y.-W.; Chen, M.-C.; Lin, Y.-J.; Huang, H.; Ortiz, R. P.; Stern, C.; Chung, M.-C.; Feng, C.-Y.; Chen, L.-H.; Facchetti, A.; Marks, T. J. Versatile α,ω-Disubstituted Tetrathienoacene Semiconductors for High Performance Organic Thin-Film Transistors. *Adv Funct Mater* **2012**, *22*, 48-60.

(94) Hestand, N. J.; Spano, F. C. Molecular Aggregate Photophysics beyond the Kasha Model: Novel Design Principles for Organic Materials. *Accounts of Chemical Research* **2017**, *50*, 341-350.

(95) Spano, F. C. The Spectral Signatures of Frenkel Polarons in H- and J-Aggregates. *Accounts of Chemical Research* **2010**, *43*, 429-439.

(96) Fauvell, T. J.; Zheng, T. Y.; Jackson, N. E.; Ratner, M. A.; Yu, L. P.; Chen, L. X. Photophysical and Morphological Implications of Single-Strand Conjugated Polymer Folding in Solution. *Chem Mater* **2016**, *28*, 2814-2822.

(97) Fauvell, T. J.; Cai, Z.; Kirschner, M. S.; Helweh, W.; Kim, P.; Zheng, T.; Schaller, R. D.; Yu, L.; Chen, L. X. Effects of Intra- and Interchain Interactions on Exciton Dynamics of PTB7 Revealed by Model Oligomers. *Molecules* **2020**, *25*, 2441.

(98) Szarko, J. M.; Rolczynski, B. S.; Lou, S. J.; Xu, T.; Yu, L.; Chen, L. X. Photovoltaic Functions of Intramolecular Charge Transfer Copolymers: Exciton and Charge Transfer Dynamics Studies of PTB7. *Adv. Func. Mat.* **2013**, *DOI: 10.1002/adfm.201301820*

(99) Li, C.; Li, Y.; Xu, L. X.; Meng, R. X.; Gao, K. Exciton-to-Charge Dynamics Driven by the Nonuniform Polymer Packing at Donor/Acceptor Interfaces. *J Phys Chem C* **2020**, *124*, 1898-1906.

TOC Figure and text

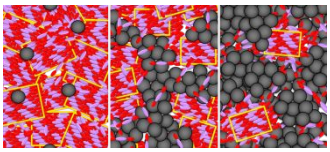

Exciton evolution with $PC_{61}BM$ loading in small molecule BHJ layers revealed by GIWAXS and ultrafast optical transient absorption spectroscopy.